# $J/\Psi$ Production Measurements by the Muon Arms in Run-III

M. Brooks, N. Bruner, J.M. Burward-Hoy, V. Cianciolo, Y. Cobigo,
O. Drapier, F. Fleuret, S. Gadrat, J. Gosset, R. Granier de Cassagnac,
R. Hobbs, N. Kamihara, S. Kelly, D.J. Kim, M.J. Kweon, P. McGaughey,
M.J. Leitch, J. Nagle, G. Roche, H. Sato, D. Silvermyr, V.N. Tram, X. Wang, C. Zhang

January 23, 2004

**Abstract**

We present here the results of differential cross section measurements, $\frac{d\sigma_{J/\psi}}{dy}$ for $J/\psi$ production from d-Au and p-p collisions, as well as the ratio between dAu and pp (nuclear modification factor) at $\sqrt{s}$ = 200 GeV in Run-III. The $J/\psi$s were measured in the South and North muon arms over a $J/\psi$ absolute rapidity range of approximately (1.2, 2.2) and the data that were analyzed were taken from the Run III dimuon-triggered data. This is a very similar analysis to what was done for Run II p-p, so we also refer to [1] for additional information. Advanced non cross-section analyses, such as polarization for p-p, are deferred to future analysis notes.

## 1 Introduction

A lot of the interest regarding the Run-III dAu and pp data is focused on the effects of shadowing and/or cold nuclear matter effects. These are interesting in themselves (see results from e.g. FNAL program where some of us have participated), and are also essential for comparisons with AuAu results.

In this section, the ingredients needed for the measurements are listed. In the following sections, the data sets, the analysis and the estimates for these various factors will be described.

The equation for $\sigma_{tot}(AB \to J/\psi \to \mu^+\mu^-)$ (with the correction factors in the chosen factorization; AB in our case being dAu or pp) is given by:

$$\sigma_{J/\psi}^{tot} = \frac{N_{J/\psi}}{A\ \varepsilon_{J/\psi}^{4\pi}\ B_{\mu\mu}\ \varepsilon_{BBC}^{J/\psi}} / \frac{N_{MB}}{\sigma_{tot}^{AB}\ \varepsilon_{BBC}^{MB}} \tag{1}$$

where

- $N_{J/\psi}$ = the number of $J/\psi$s reconstructed in the muon arm that pass our given cuts (listed in section 3.8), in particular a vertex cut at $\pm$38 cm.
- $A$ = the detector acceptance for J/$\psi$'s thrown over $4\pi$.
- $\varepsilon_{J/\psi}^{4\pi}$ = the reconstruction efficiency for J/$\psi$'s thrown over $4\pi$ with a vertex within $\pm$38 cm. For this particular calculation each event was also required to pass the simulated di-muon trigger.
- $B_{\mu\mu}$ = the branching ratio for $J/\psi$s decaying to two muons
- $\varepsilon_{BBC}^{J/\psi}$ = the BBC trigger efficiency for $J/\psi$ events produced within acceptable vertex limits ($\pm$30 cm).
- $N_{MB}$ = the number of minimum bias events used for this analysis, that have an event vertex within acceptable vertex limits ($\pm$38 cm).
- $\sigma_{tot}^{AB}$ = the AB (= pp or dAu) total cross section at $\sqrt{s} = 200$ GeV.
- $\varepsilon_{BBC}^{MB}$ = the BBC trigger efficiency for minimum bias events that have a vertex within acceptable vertex limits ($\pm$30 cm).

# 2 Data Set and Running Conditions

## 2.1 Run III Data Set

Online Event Selection — Events were selected by the coincidence of a valid minimum bias (BBCLL1) trigger and a valid MUID Blue Logic (dimuon) Trigger (BLT) which is described in section 2.5 Almost all events which passed the dimuon trigger for selected runs were filtered out of the full data set and written to separate PRDF files. More info is given in filtering section 3.6.

## 2.2 State of Muon Tracker during Run III

During Run III both the south and north muon tracker arms were installed and taking data. There were some high voltage channels in the tracking chambers which were disabled because of high current draw, a handful of data packets with intermittent problems, and a few packets which were found to have bad data (duplicated channels) in them. For the selected runs, all packets were in, and basically the same HV channels were off, i.e. we have a fairly stable situation throughout the analyzed data. We attempted to account for the problems in the Monte Carlo and real data analyses.

## 2.3 State of Muon Tracking Alignment for Run III Analyses

The alignment of the three tracking stations relative to each other was determined by looking at straight tracks from field-off data that were taken during Run III. Once the relative alignment was determined, correction constants were produced to be used for both the Monte Carlo detector response and the reconstruction of both Monte Carlo and real data.

The alignment procedure was basically the same as for the Run II analysis. The expected phi alignment accuracy is approximately 100 $\mu$m. The remaining misalignment errors contribute little to the $J/\psi$ mass resolution.

## 2.4 State of Muon Identification during Run III

In general, the status of the MuID HV was good during Run-III. However, there were some bad chains where HV could not be applied at all or we could apply only lower voltage (less than 4300V) due to some problems. Also, there were issues with beam-related background, specially in the beginning of stores, which caused high current draws. Therefore, the MuID HV was left off until beam conditions were stable. (For Run IV, shielding is being installed to alleviate this problem). During the later part of the dAu run, there were some issues regarding the BLT crate (a bad LV module that was later replaced) that caused a drop in the so-called Trigger Circuit Efficiency (TCE) in the North arm. Furthermore, for the p-p running, the noise in the South MUID became worse, and forced running with higher thresholds (120 instead of 90, mV), leading to a reduced efficiency.

The general procedure of how the MuID efficiencies were estimated, as for Run II, using roads reconstructed for minimum bias events is summarized in [2]. In addition to this procedure, alternative methods were also used for independent estimates/cross-checks, including using reconstructed tracks from the MuTR in the new framework, with momentum and depth cuts, comparing projections and hits in the MuID. Since more severe cuts are applied than was used in the trigger, this method can be used on triggered data, which is very beneficial in terms of statistics. These corrections are large contributors to the overall efficiency corrections and systematic errors, and are described in detail in section 4.2.

## 2.5 Dimuon Trigger used during Run III

The so-called MuID Blue-Logic Trigger was used for Run-III. The trigger scheme and its performance (in Run-II) are summarized in [3]. For the selected runs in Run-III, the last gap was not used in the trigger, due to the large beam background mentioned earlier. Therefore, the so-called Deep trigger was more of a shallow Deep trigger, sometimes referred to as Sheep and going to the fourth gap. The shallow trigger was going to the second gap. For the later third of the collected d-Au luminosity, we filtered on the 2-Deep trigger, while for the earlier parts of the d-Au run, and for the p-p run, the dimuon trigger was 1D1S.

The trigger circuit efficiency from the pp dimuon trigger for the runs we analyzed is shown in figures 1 and 2. The red line indicates 95% efficiency.

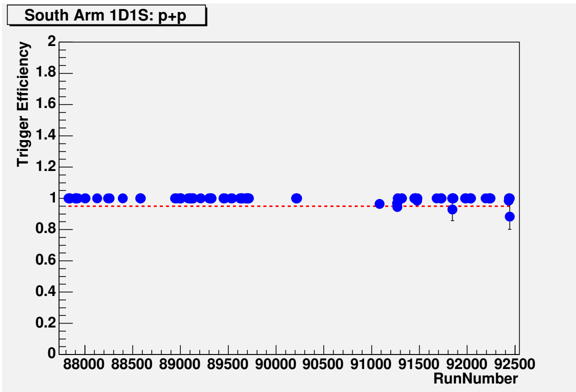


Figure 1: Trigger Circuit Efficiency for South dimuon trigger in p + p

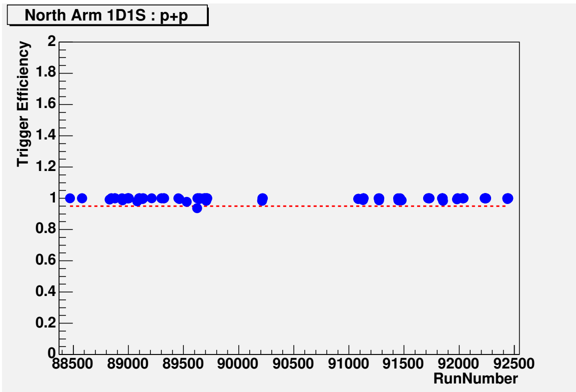


Figure 2: Trigger Circuit Efficiency for North dimuon trigger in p + p

## 2.6 Selection of Good Runs

In order to minimize the systematic error due to varying Muon Tracking HV, Muon Identification HV and Muon Tracking electronics problems, only those runs that passed the cuts shown in table 1 were selected for the analysis. A further elimination of runs was made based on examination of the hit distributions and occupancies from online monitoring and the PHENIX logbook. The rejected runs are also addressed in the run selection part of the analysis web page [4] along with the reasons for their rejection.

In run 3, the Muon Tracking HV performed well and effects from the few bad HV channels are small. Also most runs that did have a problem are ones that already had problems with Muon Identification HV. Next runs which have a large number of bad Muon Identifier HV channels have been eliminated according to the cuts which are listed in table 1.

Because the efficiency loss from these bad Muon Identifier HV runs was found to be quite large, a calculation of the effect of the bad HV on the overall efficiency has been done for each run, and runs with more than 80% loss have been thrown out. Finally some runs had high occupancy and high multiplicity in some MuTR packets and were excluded from the analysis. This problem was caused by unstable low voltage distribution cards.

The final list of good runs used in the analysis for d-Au is listed in table 3 (North 2D), table 4 (South 2D), table 5 (North 1D1S) and table 6 (South 1D1S) and for the p-p runs is listed in table 7 (North 1D1S) and table 8 (south 1D1S).

| Run | MuTR HV | Mutr Electronics | MuID HV |
|---|---|---|---|
| dAu(south) | 9( 3) out of 160 | 2 octants missing(0) | 40(32) out of 300 |
| dAu(north) | 20(11) out of 160 | 2 octants missing(0) | 35(25) out of 300 |
| pp(south) | 9( 3) out of 160 | 2 octants missing(0) | 35(33) out of 300 |
| pp(north) | 20(11) out of 160 | 2 octants missing(0) | 31(25) out of 300 |

Table 1: Summary table of the maximum number of disabled MuTR and MuID HV chains allowed, and the maximum loss of the MuTR packets allowed. (X) is the nominal number of disabled chains (missing packets) for normal runs.

| Beams | Arm | Nominal ($nb^{-1}$) | Filtered ($nb^{-1}$) | MuID HV ($nb^{-1}$) | MuTr HV ($nb^{-1}$) | TCE ($nb^{-1}$) | MuTr FEE ($nb^{-1}$) | Final ($nb^{-1}$) |
|---|---|---|---|---|---|---|---|---|
| dAu | S | 2.74 | 2.36 | 1.99 | 2.33 | | 2.29 | 1.63 |
| dAu | N | 2.74 | 2.46 | 2.31 | 2.43 | | 2.36 | 1.86 |
| pp | S | 352 | 259 | 234 | 245 | 240 | 228 | 208 |
| pp | N | 352 | 233 | 199 | 219 | 195 | 223 | 184 |

Table 2: Summary of integrated luminosity ($nb^{-1}$) for final good runs and breakdown of losses for different problems.

| | | | | | | | | | |
|---|---|---|---|---|---|---|---|---|---|
| 78402 | 78511 | 78512 | 78532 | 78553 | 78808 | 78810 | 78817 | 78838 | 79047 |
| 79048 | 79050 | 79066 | 79067 | 79340 | 79341 | 79560 | 79579 | 79603 | 79615 |
| 79626 | 79629 | 79630 | 79641 | 79642 | 79643 | 79740 | 79749 | 79750 | 79762 |
| 79764 | 79765 | 79768 | 79863 | 79866 | 79872 | 79875 | 79885 | 79888 | 79960 |
| 79961 | 79962 | 79963 | 79964 | 80127 | 80139 | 80312 | | | |

Table 3: List of runs used for the d-Au analysis. North(2D)

# 3 Muon Software

The Monte Carlo codes described below were needed to calculate $A \times \varepsilon^{4\pi}_{J/\psi}$ for $J/\psi$'s falling in the rapidity and $p_\perp$ bins of interest to our calculations. The reconstruction code that was used was common to Monte Carlo and real data analyses. We attempt to describe the level of detail included in these codes and show how well we believe they represent our real detector performance.

We used PISA2000, the PHENIX detector simulation package, with the 3D magnetic field map, July 11 (2003) version, to track the muons through the active detector volume. In PYTHIA, events were thrown at $z_{vtx} = 0$. We used PISA to simulate a Gaussian $z_{vtx}$ distribution with $\sigma = 39$ cm and only used events within 38 cm of z=0 to calculate efficiencies.

## 3.1 Muon Tracker Detector Response

The muon tracker detector response was simulated with the following:

| | | | | | | | | | |
|---|---|---|---|---|---|---|---|---|---|
| 78511 | 78512 | 78553 | 78810 | 78817 | 78838 | 79047 | 79048 | 79050 | 79066 |
| 79067 | 79340 | 79341 | 79603 | 79615 | 79629 | 79630 | 79642 | 79643 | 79749 |
| 79750 | 79762 | 79764 | 79765 | 79768 | 79863 | 79866 | 79872 | 79875 | 79885 |
| 79888 | 79961 | 79962 | 79963 | 79964 | 80128 | 80139 | 80141 | 80150 | |

Table 4: List of runs used for the d-Au analysis. South(2D)

| | | | | | | | | | |
|---|---|---|---|---|---|---|---|---|---|
| 72336 | 72350 | 72352 | 72357 | 72359 | 72361 | 72364 | 72366 | 72462 | 72467 |
| 72476 | 72482 | 72489 | 72495 | 72601 | 72603 | 72605 | 72647 | 72648 | 72662 |
| 72667 | 72669 | 72675 | 72733 | 72735 | 72737 | 72739 | 72741 | 72745 | 72749 |
| 72750 | 72756 | 72758 | 72966 | 72968 | 72971 | 73042 | 73051 | 73052 | 73053 |
| 73054 | 73057 | 73058 | 73059 | 73060 | 73061 | 73072 | 73075 | 73077 | 73082 |
| 73125 | 73127 | 74405 | 74406 | 74407 | 74410 | 74413 | 74417 | 74420 | 74425 |
| 74428 | 74443 | 74448 | 74463 | 74475 | 74477 | 74479 | 74530 | 74539 | 74558 |
| 74660 | 74662 | 74664 | 74669 | 74674 | 74675 | 74678 | 74680 | 74683 | 74684 |
| 74686 | 74691 | 74852 | 74854 | 74855 | 74857 | 75377 | 75379 | 75399 | 75403 |
| 75549 | 75747 | 75794 | 75795 | 75800 | 75983 | 76050 | 76053 | 76070 | 76073 |
| 76276 | 76284 | 76763 | 76864 | 76981 | 76983 | 76985 | 76995 | 77256 | 77266 |
| 77312 | 77313 | 77314 | 77319 | 77320 | 77322 | 77324 | 77326 | 77380 | 77520 |
| 77521 | 77531 | 77533 | 77547 | 77678 | 77683 | 77686 | 77688 | 78181 | 78182 |
| 78207 | 78208 | 78209 | 78210 | 78213 | 78269 | 78270 | 78306 | 78307 | |

Table 5: List of runs used for the d-Au analysis. North(1D1S)

- The real detector geometry was used including final alignment corrections.
- The configuration of tripped high voltage (HV) channels in the MuTr was simulated.
- DCM channels that were determined to contain bad/unreliable data were disabled in the simulated data as well as the real data analysis.
- Gains and pedestals determined from real data were used to set charge spectra and noise levels for each readout channel. If zero or minimal gain was measured from real data, the channel was effectively disabled for both MC simulations and real data analysis.
- Cathode strips in the station 2 North chambers which were determined to be scratched within the active volume were given reduced charge values, as was seen in real data.
- For the charge deposition in a tracker chamber, the Landau scale = 15.0 and the offset = 30.0 which makes the landau distributions from Monte Carlo approximatley match the landau distributions from real data.
- The value for tracker chamber efficiency was 99%

## 3.2 Event Reconstruction

For run 3 data taking we found that a number of cathode strips in Station 2 North chambers were apparently scratched in the active volume of the chamber. This resulted in reduced charge collection on these strips. We attempted to determine all such strips using real data and tagged the affected strips in the database. Then in the reconstruction code all of these strips were given a large RMS value when fitting clusters and determining the resolution of fitted clusters. This should result in more accurate chi-square values and slightly improved cluster fitting results in some cases, but we don't expect too much improvement in the final mass resolution because of the lost charge information.

| | | | | | | | | | |
|---|---|---|---|---|---|---|---|---|---|
| 72336 | 72340 | 72350 | 72352 | 72357 | 72359 | 72361 | 72364 | 72467 | 72476 |
| 72482 | 72489 | 72495 | 72603 | 72605 | 72662 | 72667 | 72669 | 72675 | 72733 |
| 72735 | 72737 | 72739 | 72741 | 72745 | 72749 | 72750 | 72756 | 72758 | 72966 |
| 72968 | 72971 | 73042 | 73051 | 73052 | 73053 | 73054 | 73057 | 73058 | 73059 |
| 73060 | 73061 | 73072 | 73075 | 73077 | 73082 | 73125 | 73127 | 74405 | 74406 |
| 74413 | 74417 | 74420 | 74425 | 74428 | 74443 | 74448 | 74463 | 74475 | 74477 |
| 74479 | 74530 | 74539 | 74558 | 74662 | 74664 | 74680 | 74683 | 74684 | 74686 |
| 74691 | 74743 | 74744 | 74746 | 74844 | 74852 | 74854 | 74855 | 74857 | 75377 |
| 75379 | 75399 | 75401 | 75403 | 75532 | 75533 | 75547 | 75549 | 75747 | 75794 |
| 75795 | 75796 | 75800 | 75983 | 76050 | 76053 | 76070 | 76073 | 76276 | 76284 |
| 76763 | 76864 | 76983 | 76985 | 76995 | 77256 | 77266 | 77312 | 77313 | 77314 |
| 77320 | 77322 | 77324 | 77326 | 77374 | 77380 | 77392 | 77521 | 77533 | 77547 |
| 77683 | 77686 | 77688 | 78181 | 78182 | 78207 | 78208 | 78209 | 78210 | 78213 |

Table 6: List of runs used for the d-Au analysis. South(1D1S)

| | | | | | | | | | |
|---|---|---|---|---|---|---|---|---|---|
| 88471 | 88578 | 88580 | 88829 | 88845 | 88846 | 88875 | 88877 | 88879 | 88943 |
| 88946 | 88993 | 88995 | 88997 | 88999 | 89003 | 89005 | 89080 | 89096 | 89098 |
| 89100 | 89128 | 89130 | 89135 | 89211 | 89299 | 89303 | 89321 | 89323 | 89325 |
| 89453 | 89463 | 89529 | 89624 | 89626 | 89629 | 89634 | 89644 | 89646 | 89648 |
| 89685 | 89693 | 89695 | 89697 | 89707 | 89709 | 89711 | 89713 | 89715 | 90213 |
| 90215 | 90219 | 91084 | 91085 | 91087 | 91126 | 91128 | 91130 | 91132 | 91134 |
| 91270 | 91273 | 91275 | 91447 | 91449 | 91460 | 91462 | 91464 | 91478 | 91718 |
| 91720 | 91726 | 91729 | 91731 | 91844 | 91846 | 91848 | 91851 | 91853 | 91979 |
| 91985 | 91987 | 92030 | 92034 | 92036 | 92038 | 92040 | 92230 | 92232 | 92234 |
| 92236 | 92238 | 92240 | 92242 | 92244 | 92436 | 92438 | 92440 | 92444 | 92446 |

Table 7: List of runs used for the p-p analysis. North(1D1S)

The old framework software reconstruction was run in the default mode which uses found muon identifier roads to seed the track finding in the track finder. By default only "golden" roads in the muon identifier are passed to the tracker to find associated tracks (see explanation of golden roads in [6]). After the tracker pattern recognition is completed, all found tracks are fit using a Kalman Filter fit package from GEANE. All muon tracker measurements as well as the measured vertex point and the muon identifier measurements are used in the fit. Following this fit a second-pass road finder module is executed which attempts to flag ghost tracks by setting the ghostflag to 1.

### 3.3 Muon Tracking Software Performance

The state of the Muon Tracker during data taking was modeled in the Monte Carlo as outlined in section 3.1. To check that the Monte Carlo representation accurately reflected the true state of the detector, the hit distributions in all planes were compared between Monte Carlo and real data, and the track reconstruction efficiency, as determined by pointing MuID roads to the muon tracker was compared between real data and Monte Carlo.

### 3.4 Muon Identification Software Performance

Some MUID software specifics is discussed in section 4.2, while describing how the

MUID tube and trigger efficiencies were estimated from real data, using MC data for cross-checks. The main part of MUID offline software of interest for this note is the road-finding. The material in this section is included for completeness and to help the reader understand the later sections. The MUID readout is

| | | | | | | | | | |
|---|---|---|---|---|---|---|---|---|---|
| 87829 | 87832 | 87839 | 87841 | 87843 | 87899 | 87901 | 87904 | 87906 | 87908 |
| 87910 | 87912 | 87927 | 88001 | 88006 | 88127 | 88243 | 88258 | 88396 | 88578 |
| 88580 | 88582 | 88584 | 88943 | 88946 | 88964 | 88995 | 88997 | 88999 | 89001 |
| 89003 | 89005 | 89080 | 89098 | 89100 | 89103 | 89105 | 89119 | 89128 | 89130 |
| 89135 | 89211 | 89299 | 89303 | 89316 | 89318 | 89321 | 89323 | 89325 | 89451 |
| 89453 | 89463 | 89529 | 89541 | 89624 | 89626 | 89629 | 89634 | 89642 | 89644 |
| 89646 | 89648 | 89683 | 89685 | 89693 | 89695 | 89697 | 89707 | 89709 | 89711 |
| 89713 | 89715 | 90209 | 90213 | 90215 | 90219 | 91082 | 91266 | 91268 | 91270 |
| 91273 | 91275 | 91316 | 91318 | 91447 | 91449 | 91452 | 91457 | 91460 | 91462 |
| 91464 | 91476 | 91478 | 91681 | 91720 | 91726 | 91729 | 91731 | 91842 | 91844 |
| 91846 | 91848 | 91851 | 91853 | 91855 | 91979 | 91985 | 91987 | 92030 | 92034 |
| 92036 | 92038 | 92040 | 92194 | 92230 | 92232 | 92234 | 92236 | 92240 | 92242 |
| 92244 | 92434 | 92436 | 92438 | 92440 | 92444 | 92446 | | | |

Table 8: List of runs used for the p-p analysis. South(1D1S)

on a digital yes/no basis; if the signal on a tube is above a set threshold, the tube is said to have fired. This reduces the problem of hit- and cluster-finding to investigating which tubes have fired, and if they are neighbors. A tube is oriented in either the horizontal or vertical direction.

The offline roadfinder in use starts out by doing 1Dim-road reconstruction. This means looking at combinations between fired tubes in the MUID planes/gaps in one orientation at a time, and keeping combinations that roughly point back to the nominal vertex position. Different search orders are used to remove possible biases. The basic requirements are that there needs to be at least one hit in one of the first two planes (0 or 1), and that the road should make it at least to plane 2. There is also a requirement that there should be at least 3 hits per 1Dim road, which for the shallower road (depth = 2) means that all planes need to be hit. This is sometimes referred to as the original parameter setting. In a reconstruction pass, this hit requirement was changed to allow for one skipped/missed plane. This is referred to as the relaxed parameter setting.

After the 1Dim roadfinding is done, the results from the two orientations are combined, into 2Dim roads. The depth, and the number of hits, between the 1Dim roads resulting in a 2Dim road need to match within $\pm 1$. In the roadfinder, there is also grouping of nearby candidate roads, and selection of so-called golden roads, but this distinction is not relied on in the offline data analysis, so we will not go into these details here.

It is to be noted that in this procedure, the reconstructed tracks have to reach the third MUID gap, while the 1D1S trigger was requesting one track to the second, and one to the fourth. As it was first seen with the new framework reconstruction (MUTOO, MUIOO) then with a modified MUI road finding, there are some $J/\psi$'s to be gained considering these shallower roads. However, because of a higher background and a lack of time to shrink it, we restrict ourselves for now to this third gap roads, the loss being taken cared of by the acceptance$\times$efficiency correction.

### 3.5 Muon Identification Trigger Simulation

To monitor the Blue-Logic Trigger online, a software Blue-logic Trigger emulator was written. It simulates the logic of hardware Blue-Logic trigger circuit and calculates trigger decisions according to Muon Identifier raw hit information we recorded online. During Run 3, we ran this emulator simultaneously with data taking and used it as a tool to diagnose Blue-Logic trigger hardware. To quantify how well the hardware works, we defined Trigger Circuit efficiency as the percentage of the times when hardware fires a trigger to the times when emulator fires a trigger. For most of the data we took, this efficiency is about 90% (again, for the p-p period, see figures 1 and 2). During offline analysis, we also use it as one of criteria for run selection.

The validity of the trigger emulator was intensively checked, already for Run-2 (see [3]) for many runs. The trigger emulator, using estimated MUID tube efficiencies, was an integral part of the simulation chain.

### 3.6 Filtering

For this analysis we use level-1 trigger filtered events for either two-deep (2D) road triggers or one-deep and one-shallow (1D1S) road triggers. For the d-Au data runs 78402-80312 we use 2D triggers, while for the earlier d-Au runs, 72336-78307, we use 1D1S triggers. For p-p runs we use only 1D1S triggers. Triggers were filtered out on the RCF machines using HPSS to extract the prdf files and the standard OnCal filtering routines to select the triggered events via the live bits with TriggerHelper. These events were then written out to separate filtered PRDF files and stored in HPSS at,

- /home/leitch/filter/MUIDN - North 2D d-Au
- /home/leitch/filter/MUIDS - South 2D d-Au
- /home/leitch/filter/MUIDN_1D1S - North 1D1S d-Au
- /home/leitch/filter/MUIDS_1D1S - South 1D1S d-Au
- /home/phnxsink/run3/run3ppfiltered_data/MUIDN - North 1D1S p-p
- /home/phnxsink/run3/run3ppfiltered_data/MUIDS - South 1D1S p-p

See also http://www.phenix.bnl.gov/phenix/WWW/run/03/dataprod/run3pp_evfilter/datasittingstatus/run3pp_datasitting.html

Note that the p-p files are small (not merged) segmented files. They were merged before to be sent to the french computing center (CCF). All the resulting merged PRDF files were transfered to HPSS at CCF using BBFTP (average rate is 3 MB/s) for reconstruction and analysis up to the nanodst's.

### 3.7 Data Production and Analysis

We built up standard dsts and MWG nanodsts from the prdfs, including the following subsystems : BBC, ZDC, FCAL, MUTR and MUID, and using the new 3D simulated field map (including the north field). Several processing passes were done to test various improvements of the reconstruction. The data we show here were processed at CCF using the pro.43 libraries. To cope for a few percents loss of segments at various stages of the analysis (mostly missing segments from the database) we correct our result by the nanodst / run control number of triggered events ratio (see table 9).

| Sample | In RC | In MWG | MWG/RC | BBC live | $\|z_{vtx}\| < 38$ | $N_{MB}$ |
|---|---|---|---|---|---|---|
| S2D | 2 412 354 | 2 217 582 | 91.93% | 1 335 801 768 | $\sim$ 96.4% | $1.184 \times 10^9$ |
| S1D1S | 31 820 276 | 27 886 566 | 87.64% | 1 875 636 515 | $\sim$ 94.5% | $1.566 \times 10^9$ |
| N2D | 1 061 717 | 1 022 462 | 96.30% | 1 701 932 446 | $\sim$ 95.2% | $1.553 \times 10^9$ |
| N1D1S | 3 051 636 | 2 847 592 | 93.31% | 1 971 994 519 | $\sim$ 94.7% | $1.711 \times 10^9$ |
| SPP | 1 164 526 | 1 164 244 | 99.98% | 4 639 768 393 | $\sim$ 97.7% | $4.531 \times 10^9$ |
| NPP | 4 062 648 | 4 057 461 | 99.87% | 4 108 647 407 | $\sim$ 98.0% | $4.021 \times 10^9$ |

Table 9: Number of processed triggers found in the run control and in the nanodst. The number of corresponding minimum bias events $N_{MB}$ is equal to the number of lived BBC triggers $\times$ the MWG/RC ratio $\times$ the fraction of these events passing our $|z_{vtx}| < 38$ vertex cut estimated on scaled recorded BBC triggers. This numbers were computed on a run by run basis and sum up to the number in the last column.

The nanodsts were then analyzed with the **offline/analysis/MWGana** package, which produces analysis ntuples (known among ourselves as picodsts). The plots were produced applying the cuts describe in the following section on these dimuons ntuples.

The picodsts used in this analysis can be found in /phenix/data25/picoDSTs/ :

- picoDST_pp03N_GoodRuns_pro43.root, picoDST_pp03S_GoodRuns_pro43.root,

- picoDST_dAu03N2D_GoodRuns_pro43.root, picoDST_dAu03S2D_GoodRuns_new3.root,
- picoDST_dAu03NDS_GoodRuns_pro43.root and picoDST_dAu03SDS_GoodRuns_pro43.root.

The south 2D one was produced with the "new" set of libraries (from the 22nd of July) which was identical to the pro.43 (from the 12th of August) as far as the muons are concerned. A bunch of files were processed with pro.43 to confirm this. Two additional comments concerning nanodsts:

- The MWG nanodsts coming out of the RCF production gives similar yields to the one we had with the CCF pass.
- A new set of nanodsts with the shallower roadfinding are available for some of the samples (and will be for the others) in the same directory, labelled pro.48 (dAu) and pro.50 (pp).

### 3.8 Analysis cuts

Several analysis cuts are made on the final ntuples in order to reduce the number of ghost tracks and to improve the signal to noise for the $J/\psi$ mass peak by reducing the background levels:

- Muon pairs with tracks flagged as ghosts by the second pass roadfinder (ghostflag = 1) are removed.
- The vertex is required to be within 38 cm of z=0, $|z_{BBC}| < 38$ cm. To deal with the acceptance loss caused by this cut, we compute the fraction of scaled bbc triggers within our vertex range and include the drop in the luminosity normalization (see table 9).
- Pairs with one or two tracks with a poor Chi-square are removed, $\chi^2/DF < 20$.
- Both tracks are required to have positive momentum (North arm, positive rapidity) or negative momentum (South arm, negative rapidity).
- $J/\psi$ rapidity has to be within $-2.2$ to $-1.2$ for the south arm and $+1.2$ to $+2.4$ for the north arm.
- The difference between the dimuon reconstructed vertex and BBC vertex is required to be less than 25 cm ($|z_{BP} - z_{BBC}| < 25$ cm).
- The two roads have to come from different quadrants.

Except for the vertex cut which is taken cared of in the luminosity computation, all these cuts are applied to the montecarlo reconstruction when we compute the acceptance correction.

## 4 Efficiency estimates

### 4.1 Muon Tracker

The muon overall tracker efficiency for $J/\psi$ events is evaluated along with the muon identifier and the muon trigger using a full simulation of the detector for Pythia generated $J/\psi$ events as outlined in section 3.1 to 3.5. One input to these simulations is the intrinsic efficiency of the muon tracker planes. As mentioned in 3.1 this was taken as 99%. A data driven method of evaluating this efficiency was accomplished by using good muon identifier roads to project back into the tracker and determine the efficiency for finding these tracks in the tracker. This method can be used for both simulated events and for real data events. But in the later case, one has to be very careful to select clean real roads that correspond to real tracks going all the way through the muon tracker stations. Comparisons between simulation and data at present show good agreement for the South muon tracker but only fair agreement for the North muon tracker. But further cuts on the quality of the roads seems to be converging towards good agreement for both arms. A systematic uncertainty allowing for the present state of this verification of the muon tracker plane efficiencies is included in the later section 8 about systematics.

Just as for the run2 pp analysis, we used PYTHIA v5.720 with GRV-98 parton distribution functions to generate the $J/\psi$'s used in determining our acceptant and efficiency. The $J/\psi$ could be primar or from a $\chi_c$ decay. We forced the $J/\psi \to \mu^+\mu^-$ decay with no kinematic cuts over $4\pi$. More details on this can be found in the run 2 analysis note [1].

## 4.2 Muon Identifier

We describe here the technique used to determine the Muon Identifier (MUID) tube efficiencies and the resulting values from Run 3 proton-proton and deuteron-gold data sets.

It has been observed that there were various problems with high voltage (HV) units in the MUID during Run 3. Therefore it is important to calculate tube efficiencies in quantized groups corresponding to the HV chains. In order to have sufficient statistics for this level of granularity, we have used the dimuon triggered data sampled (1D1S and 2D), but correct out this trigger bias. Below is an outline of our procedure.

1. A pass is made through all dimuon triggered data PRDF files in the “good runs” list. See earlier sections for these lists.
2. We use the MUTOO and MUIOO new framework resulting found tracks. In order to be used in the analysis, we require a track that is found in the muon tracker (MUTR) with a matched MUID road. Thus, the tracks must pass the default MUTOO track finding parameters, and more importantly the MUID road must pass the default MUIOO road finding parameters.
3. We remove any trigger and road finding algorithm bias by requiring that all hit requirements are satisfied without the plane of interest. We actually do this in code by setting that plane to have no hit and seeing that all requirements are met, and then setting that plane to have a hit and seeing that all requirements are met. Both checks are necessary because sometimes an extra hit can cause a road to be lost. For example, since the roadfinder requires agreement within +/- 1 for the number of hits in the 1Dim horizontal road and 1Dim vertical road.

We list the relevant checks to remove any bias below.

Trigger Bias Removal:

1. We assume that each track may have to have satisfied the Deep Road Blue Logic Trigger requirement (since in the 1D1S case we do not know which is shallow and which is deep ahead of time). The BLT requires 7 of 8 hits in planes 0,1,2,3 in a given quadrant.

Thus, if the plane of interest is in planes 0-3, we require all of the other 7 planes to have hits associated with the road.

Road Finding Bias Removal:

1. We use two MUIOO search seed orders (-1,2,1,0,3,4) and (-1,1,2,0,3,4). The (-1) means that the roadfinder starts with the point (x,y,z = 0,0,0) and connects to hits in the next listed plane (either 2 or 1). The roadfinder uses both search orders and then removes completely redundant roads (all hits identical). Thus, we are implicitly requiring a hit in plane (1 or 2) in both horizontal and vertical.
2. We require all MUIOO roads to have $depth == 4$. This requires a hit in either plane 4 vertical or horizontal or both. So if the plane of interest is in plane 4, we require that the other view have a hit in plane 4.
3. We require a minimum depth of each 1D road ($min\_depth\_1d >= 2$). Thus, both horizontal and vertical require at least one hit in (plane 2 or plane 3 or plane 4).
4. We require a minimum number of hits of each 1D road ($min\_nhits\_1d > 2$). Thus there must be at least 3 hits in each 1D road.
5. We require that the depth of the 1D vertical road agree with the depth of the 1D horizontal road within $\pm 1$.
6. We require that the number of hits in the 1D vertical road agree with the number of hits in the 1D horizontal road within $\pm 1$.

These are part of the standard road finding method and present a complex set of biases. We must ensure that all of these conditions are satisfied without the influence of the plane of interest.

Note that we have relaxed some of these road finding requirements in the later pass on the triggered data. However, for the efficiency studies we have left the condition on the tighter cuts.

Once the track + road candidate passes the above requirements without the plane of interest, we determine where the road falls in terms of panel number and high voltage (HV) chain.

We then just check for these roads, what percentage of the time does the plane of interest have a hit associated with the road.

#### 4.2.1 Good Run List Weighting

We have calculated the high voltage chain by chain efficiencies for every run in the "good runs" list for north and south arms. We then weight each run's efficiency by the number of sampled minimum bias events, by using the $BBCLL1 >= 1$ LIVE scaler value for that run. DongJo has noted that the more correct weighting would be $BBCLL1 >= 1$ LIVE scaler times $|zvtx| < 38/zall$ to get the correction for the number of events in the offline analysis cuts.

It is notable that this weighting, instead of just weighting by the number of tracks found (which is what both Hiroki's method and Sean's previous calculations used), avoids certain assumptions about uncorrelated panel status. If you had 50% of the run with panel 2 off in planes 0 and 1, you would never have a track for those runs and thus not count the lower efficiency. If these states are many and random, then it all averages out.

Jamie found using the run weighting for proton-proton data that this lowered the average efficiency by 0.6%.

#### 4.2.2 Random Hit Efficiency Bias

There can be cases where the particle does not leave a hit in a MUID tube due to an inefficiency, but a random other hit falls within the road finding window. This leads to an increase in the MUID efficiencies calculated. We need to remove this random hit bias because our final acceptance and efficiency calculations will be done by embedding Monte Carlo J/psi on top of real data events. The real data events have the random hit contribution already, and thus we would be double counting if we also include this contribution in the tube efficiencies.

One might also be concerned that since we analyze triggered events, they might have a bias towards larger occupancy from tunnel related background.

We have used a simple approximation to remove this random hit bias.

The MUIOO road finder associates new hits that are within ±30 cm of the current road parameters. As the roadfinder builds up 1D roads, it re-fits points already associated with the road. It then decides whether to associate a new hit if it is within this window of the current parameters projected to that plane. This adds a subtle road search order dependence to the search parameters used in the window cut.

We output an additional ntuple that contains not only the track and MUID road information, but also the residual for each MUID plane. That means we have the distance from the MUID projected road to the nearest hit in a particular plane of the MUID.

From Monte Carlo studies of single muons, we find that real hits are within ±15 cm of the final determined road finder parameters projected to the plane of interest. Thus, we break things down in the following equation.

$$totaleff = realeff + (1 - realeff) * randeff + (1 - realeff) * (1 - randeff) * randeff \qquad (2)$$

The total efficiency for finding a hit within the 30 cm window is equal to the real tube efficiency from the particle of interest (realeff). Then if the real particle does not leave a hit (1 - realeff), you may get a random hit within the 0-15 cm window (randeff). If there is no hit at all within ±15 cm, you may have a random hit within the window $|15 - 30|$ cm. We assume the probability of getting a random hit within 0-15 cm is the same as 15-30 cm. Remember that these are search windows for 1D roads. Thus, the third term in the expression above is the probability to have no hit within ±15 cm, but to have a hit within ±30 cm.

We can determine from data the (totaleff) and the last term (eff1530 = (1 - realeff) * (1 - randeff) * randeff). We then have two equations and two unknowns and can solve for the real tube efficiency that we are after (realeff).

*** We need to confirm that all real MUID hits from the track are within ±15 cm.... Hiroki's method automatically assumes this?*

*Assumptions - possible problems/issues....*

*The files Sean sent around are without the random benefit subtracted. Jamie found it lowers the average efficinecy in planes 0-3 by 1.5% and more like 3% in plane 4. This needs to be double checked (see above). Plane 4 is the most problematic. However, we do not use this plane in the trigger, and if the analysis required depth¿=3 (instead of depth ==4), we would not have almost any dependence on this particular parameter.*

#### 4.2.3 Systematic Checks

We can compare the results from triggered events with those in minimum bias events to see if there is any residual problem. We have not done this for the proton-proton results, and await the nanoDSTs from the production pass. We have done this comparison with the partial production pass for deuteron-gold and find that the results on average agree within 0.2%.

**Systematic Errors** - Current list of sources....

- ±0.2% : Trigger vs. Min.Bias comparison - not yet checked for pp
- + 0.0% - 2% : Random Hit removal assumptions - This is the present guess if we do not remove the randoms
- ±1% : Sharing between HV chains...

*** What about agreement/disagreement with cosmic ray data - there is new cosmic data available, and a cross-check will be made.***

### 4.3 Embedding studies

For realistic background and chamber occupancies, we embedded the simulated muon hits from $J/\psi$s into real dAu MinBias events in several centrality bins. The dAu files chosen for emdedding had to have the same HV state as the simulated data and a sufficient number of events. We used the runs 78838, 79863, 80312 for the HV state 79863. The difference in efficiency obtained between clean $J/\psi$ events and $J/\psi$ events embedded in real events was shown in table 10 which are statistics limited at the 3% level. Based on this we assign a systematic error from embedding of 3%. We used the same version of track reconstruction as we used for real data reconstruction for this study.

| Event Type | Arm | Thrown | Reconstructed (No emdedding) | Reconstructed (emdedding) | $A \times \varepsilon^{4\pi}_{J/\psi}$ (No emdedding) | $A \times \varepsilon^{4\pi}_{J/\psi}$ (emdedding) |
|---|---|---|---|---|---|---|
| MinBias 0-20% | South | 12451 | 659 | 653 | 5.29+-0.21% | 5.24+-0.21% |
| MinBias 20-40% | South | 14642 | 796 | 797 | 5.43+-0.20% | 5.44+-0.20% |
| MinBias 40-60% | South | 15801 | 855 | 863 | 5.41+-0.19% | 5.46+-0.19% |
| MinBias 60-88% | South | 24845 | 1309 | 1337 | 5.26+-0.15% | 5.38+-0.15% |
| MinBias 0-20% | North | 13901 | 1011 | 1023 | 7.27+-0.24% | 7.35+-0.24% |
| MinBias 20-40% | North | 16453 | 1212 | 1226 | 7.36+-0.22% | 7.45+-0.22% |
| MinBias 40-60% | North | 17684 | 1292 | 1307 | 7.30+-0.21% | 7.39+-0.21% |
| MinBias 60-88% | North | 27885 | 2030 | 2088 | 7.27+-0.17% | 7.48+-0.17% |

Table 10: Summary of the emdedding results : clean $J/\psi$ events are embedded in real dAu events in each centrality bins. errors in the table are only statictical

# 5 Fitting dimuon spectra

Applying the cuts given in section 3.8, we find the $\mu^+\mu^-$ spectra given by the red triangle histograms on figures 3 to 8 for our various data samples. $J/\psi$ peaks can clearly be seen.

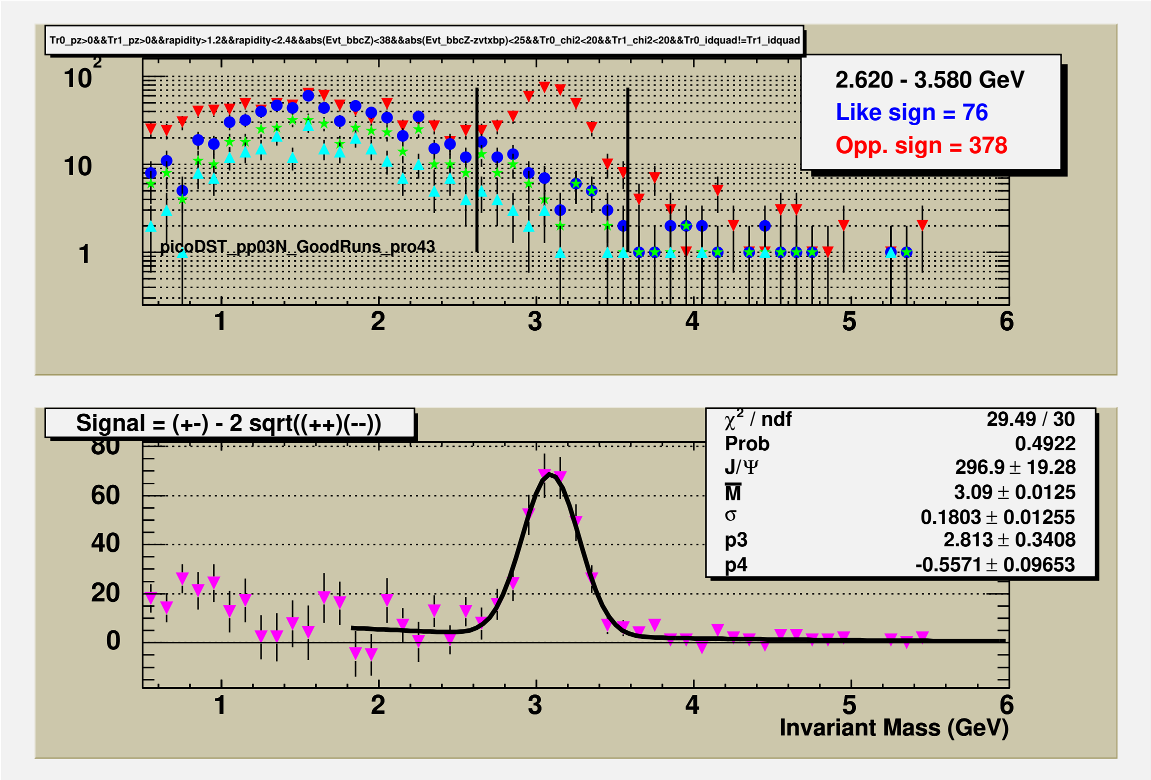


Figure 3: Invariant dimuon mass distributions for proton+proton data in the north arm. Top plot : $\mu^+\mu^-$ (red triangles), $\mu^+\mu^+$ (green stars), $\mu^-\mu^-$(light blue triangles) and $\mu^+\mu^+ + \mu^-\mu^-$ (blue circles). Bottom plot : background subtracted distribution fitted by an exponential plus a gaussian function.

## 5.1 Combinatorial background

Most of the background under the peaks is due to the combinatorics of uncorrelated muons. To subtract this background, we rely on the like sign events. The spectra of the $\mu^+\mu^+$ and $\mu^-\mu^-$ are shown in green stars and light blue triangles, the blue circles being the sum.

A rough estimate of the number of $J/\psi$ is given by the subtraction of the unlike sign to the like sign pairs in a given mass window. This method was applied for the run 2 result [1]. Given the higher statistics we have, we move to a more accurate method, to reflect that $N_{++}$ (the number of $\mu^+\mu^+$ pairs) is not equal to $N_{--}$ (the number of $\mu^-\mu^-$ pairs) as it can clearly be seen on the plots. The combinatorial background is thus determined by counting $N_{++}$ and $N_{--}$ that pass the same cuts as $N_{+-}$, and estimated with $N_{bkg} = 2\sqrt{N_{++} \times N_{--}}$.

The bottom purple triangle histogram on figures 3 to 8 is then : $N_{+-} - 2\sqrt{N_{++} \times N_{--}}$ (aka : $purple = red - 2\sqrt{green \times lightblue}$).

We're also working on two other subtraction methods :

1. One is to fit individually the $\mu^+\mu^+$ and $\mu^-\mu^-$ spectra above 2 GeV by exponentials and to build up $N_{bkg} = 2\sqrt{N_{++} \times N_{--}}$ based on the resulting functions. This shows the advantage to wash out statistical fluctuations, which are large in the high mass region.

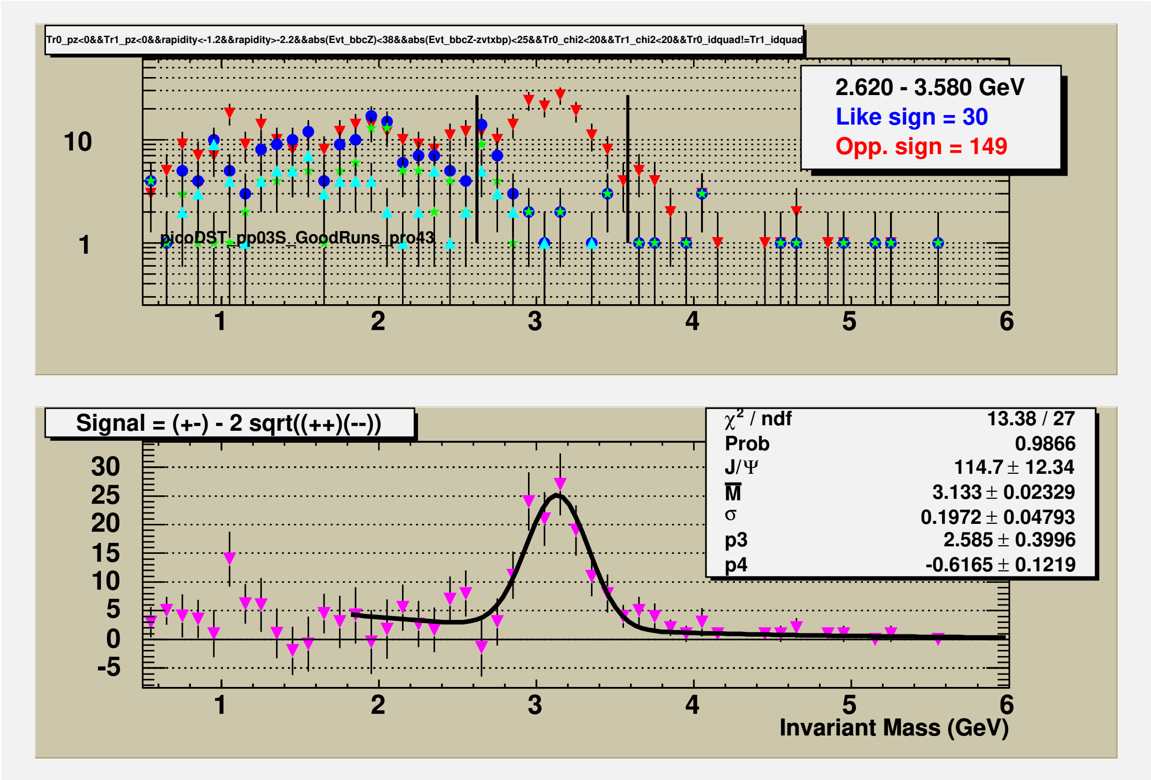


Figure 4: Invariant dimuon mass distributions for proton+proton data in the south arm.

2. However, the two methods above uses the assumption that there is no charge assymmetry introduced by the detector acceptance. An alternative approach is to build up combinatorial background by mixing single muons from different events. This method is under developpment but already shows good agreement with the $N_{bkg} = 2\sqrt{N_{++} \times N_{--}}$ method.

The differences between the fitting method 1 above and our subtraction method stays within 5% for our global samples. Higher differences are seen when we split the data in centrality, transverse momentum or rapidity bins. They all have been carefully investigated and are mostly due to changes in the physical background slope estimation, and thus are being covered by the systematic error quoted in the following section.

The method 2 gives correction factors that are also less than 5%. Thus we assign a 5% systematic error for the combinatorial background estimation and subtraction.

## 5.2 Physical background

Once we have subtracted the combinatorial background, we are left with the purple triangles bottom curves, which should mostly be made of physically correlated muons. We see on this plots that we have some signals below and above the $J/\psi$ mass region, and also a hint of the $\psi'$. Studies are being made to understand this background in terms of open charm (low mass) and Drell-Yann (high mass). For this preliminary result, we derive the number of $J/\psi$ doing a simple gaussian + exponential fit such as the ones displayed on the figures. The fits lead to reasonable masses and resolutions. The exponential slopes are consistant between the four dAu samples, and separately on the two pp samples, giving us confidence that we're fairly describing the backgrounds.

However, we have tried to fit the signal shapes with many different functions and find that they all fairly describe the data :

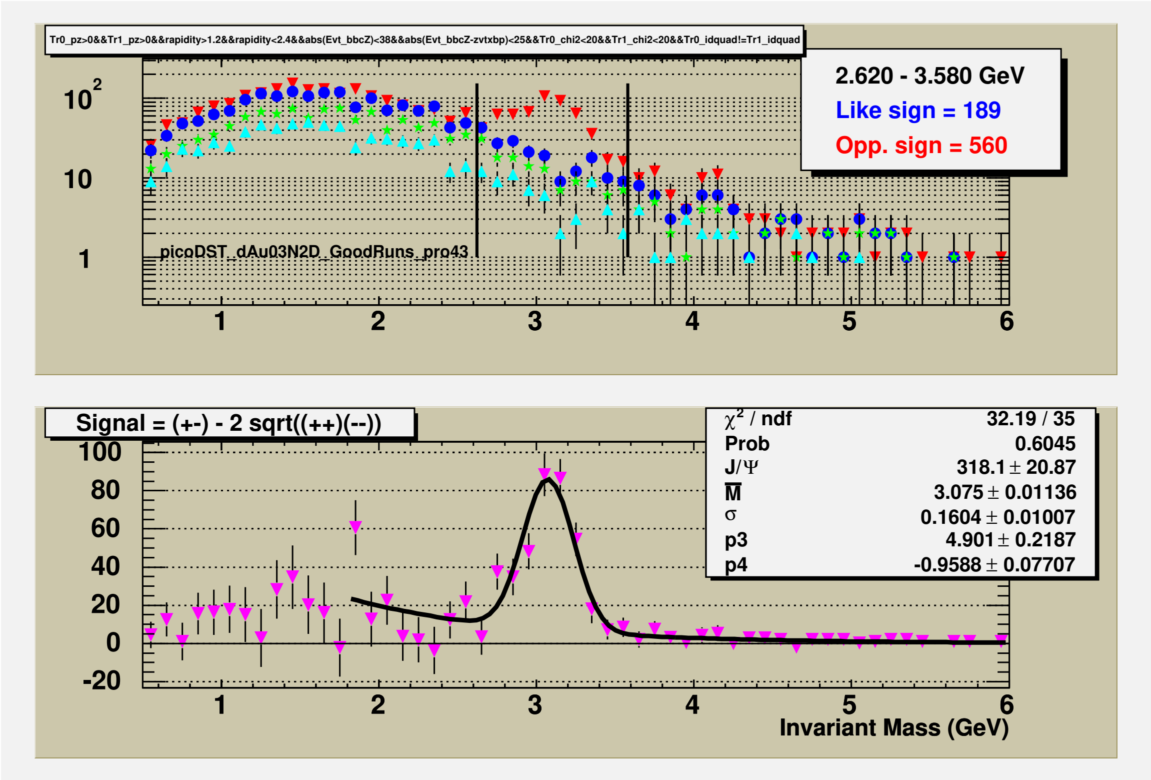


Figure 5: Invariant dimuon mass distributions for deuteron+gold data in the north arm (2D triggers).

1. Gaussian + exponential between 1.4 to 6.0 GeV (used to derive the final numbers).
2. Gaussian + exponential with a different fiting range (between 1.8 and 6.0 GeV for the plots presented here and in the table 11, but we have tried other values).
3. Gaussian + quadratic polynomial.
4. $J/\psi$ gaussian + $\psi'$ gaussian ($\Delta m$ from PDG and same resolution) + exponential.
5. $J/\psi$ gaussian + $\psi'$ gaussian ($\Delta m$ from PDG and same resolution) + 2 exponentials (low slope at high mass for Drell-Yann and high slope at low mass for open charm, both inspired from preliminary montecarlo simulation).
6. Simple Gaussian with no background, leading to results which are very close to the previous method.
7. Gaussian + an exponential constraint to fade out under the peak, basically leading to no background contribution in the $J/\psi$ mass region.

The results of all these methods are given in table 11. The two last methods give reasonnable $\chi^2$ probabilities and cannot be totally ruled out without further understanding and simulation of our backgrounds. Thus we assign for now a systematic error on our fitting procedure equal to the difference of our fit to the no background hypothesis, divided $\sqrt{12}/2$.

The methods 1 to 5 give results that are much closer from one another, the differences being far below the systematic errors computed above.

For the dAu/pp ratio, we take the differences between the highest and the lowest estimation and divide it by $\sqrt{12}$.

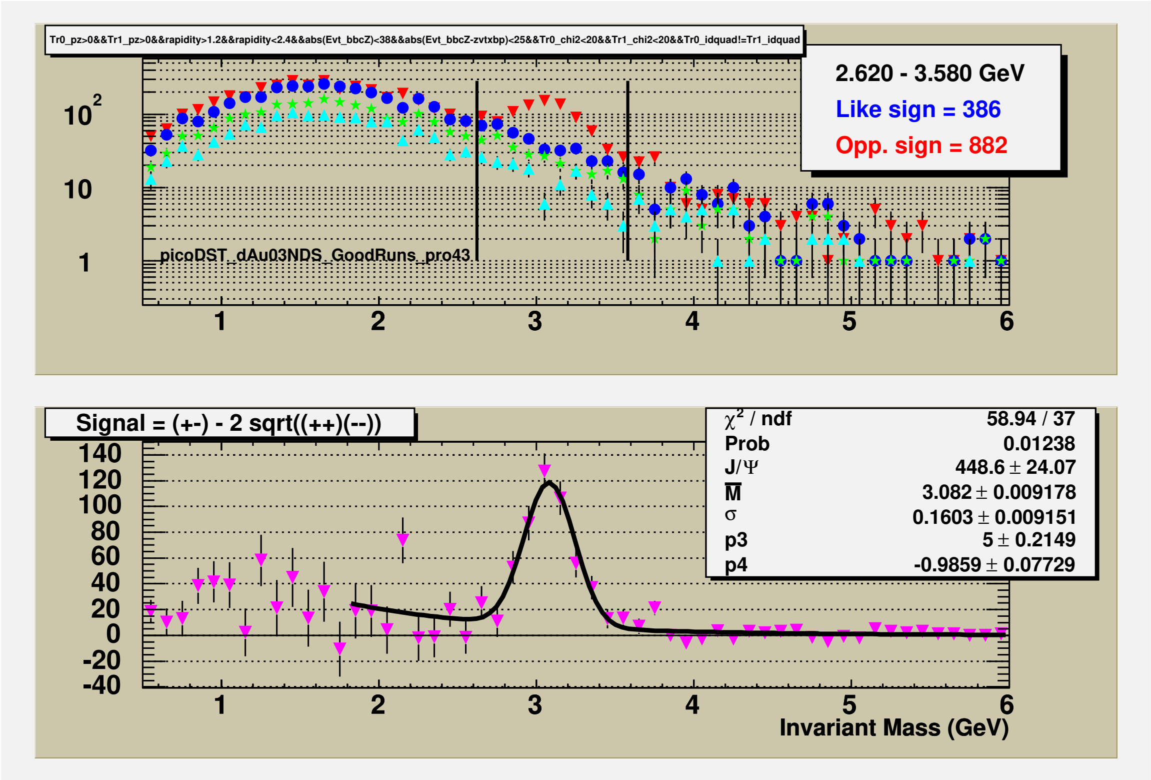


Figure 6: Invariant dimuon mass distributions for deuteron+gold data in the north arm (1D1S triggers).

**Fitting code :** A macro was developped to apply the various combinatorial and physical backgrounds fits mentionned above can be found in CVS under offline/analysis/MWGana/plots/massplot.C

### 5.3 Fitting subsamples

When we divide the data samples into rapidity, transverse momentum or centrality bins, we use the exponential + gaussian fit, applying some constraints based on the results obtained from the global sample fit. Typically, here are the constraints we have to apply to make all the fits to converge :

- Fit being done between 1.4 and 6 GeV to ease the exponential slope estimation.
- $3.05 <$ gaussian centroid $< 3.16$ GeV.
- $150 <$ sigma $< 200$ MeV.
- $0 <$ Expon. Norm $< 200$.
- $0 <$ Expon. Slope $< 3$. ($-1/p4$ in the plots)

For each binning and each sample, we checked that the sum of the numbers of $J/\psi$'s found on each bin is roughly equal to the number found on the global sample.

## 6 Centrality Selections

In this section, we address the way we divide the data sample in bins of centrality in order to compute the ratio of central to peripheral events (Rcp) and the ratio of the various deuteron+gold centrality classes to the proton proton data (Rda)

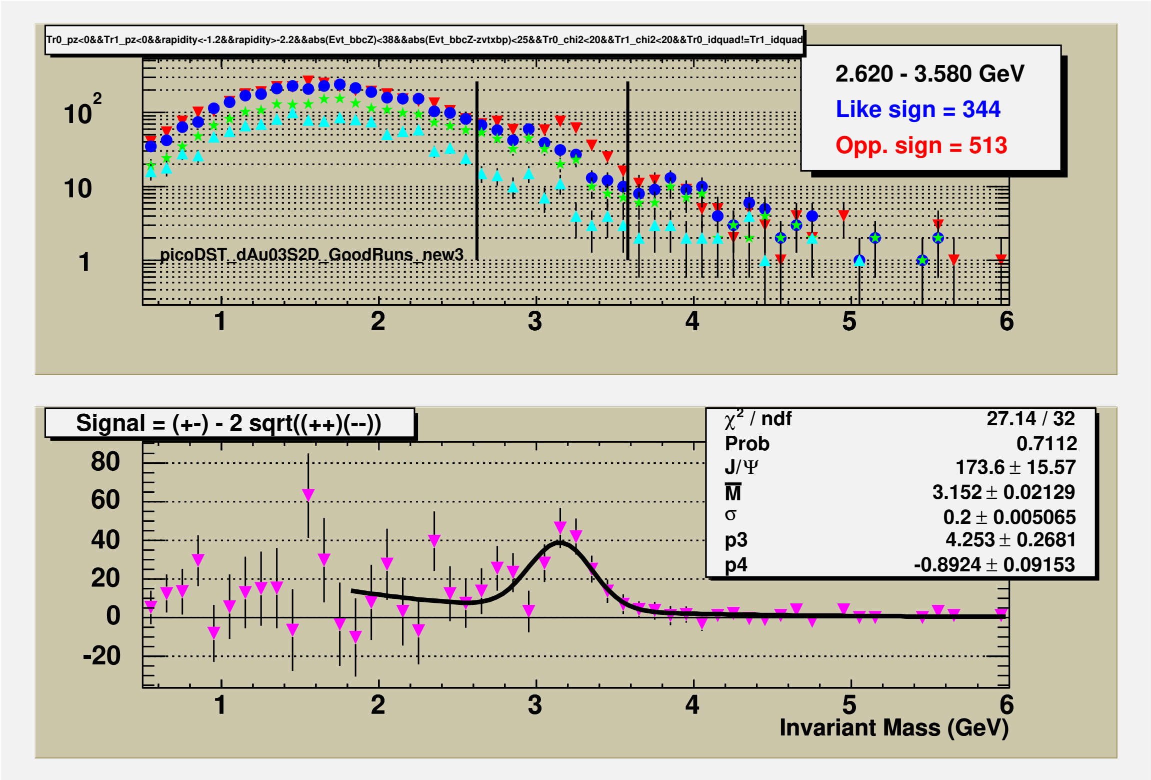


Figure 7: Invariant dimuon mass distributions for deuteron+gold data in the south arm (2D triggers).

The centrality selections are identical to those used in AN210. These selections are $0-20\%$, $20-40\%$, $40-60\%$, and $60-88\%$ centrality.

All assumptions made in An210 are also assumed here. We repeat these assumptions for completeness. These include:

1. BBC South hit multiplicity is $\approx$ the number of Au participants. In d-Au collisions, ${}^{Au}N_{part} \approx N_{coll}$.
2. BBC South hit multiplicity can be described by the Negative Binomial Distribution.
3. Assuming uncorrelated hits in the BBC South, the parameters in the negative binomial distribution are proportional to the number of Au participants.
4. A Glauber model calculation can be used to determine the number of collisions, $N_{coll}$.

For each centrality class, there is a centrality bias caused by the neutral pion $p_T \geq 1.5$ GeV trigger (described in more detail in note AN209). Of the minimum bias events, there is some fraction of events for which this high $p_T$ trigger is satisfied. This correction is calculated based on negative binomial distribution fits to the $N_{coll}$ distributions in each class. The results from AN210 are included below for completeness in Table 12.

As the muon trigger is also a high $p_T$ trigger, we apply the same corrections to our sample in the centrality results reported here. Eventually, we should determine our own corrections based on muons detected in the muon arms as the high $p_T$ trigger assumes a neutral pion detected in the central arms. In the notation of equation 1, this correction basically replaces the $\varepsilon_{BBC}^{J/\psi}/\varepsilon_{BBC}^{MB}$ ratio taken on minimum bias sample. One should note that the weighted average of the correction across centrality bins is equivalent to the minimum bias correction: $(0.2. + 0.2 \times 0.995 + 0.2 \times 0.974 + 0.28 \times 0.885)/0.88 \sim 0.96$.

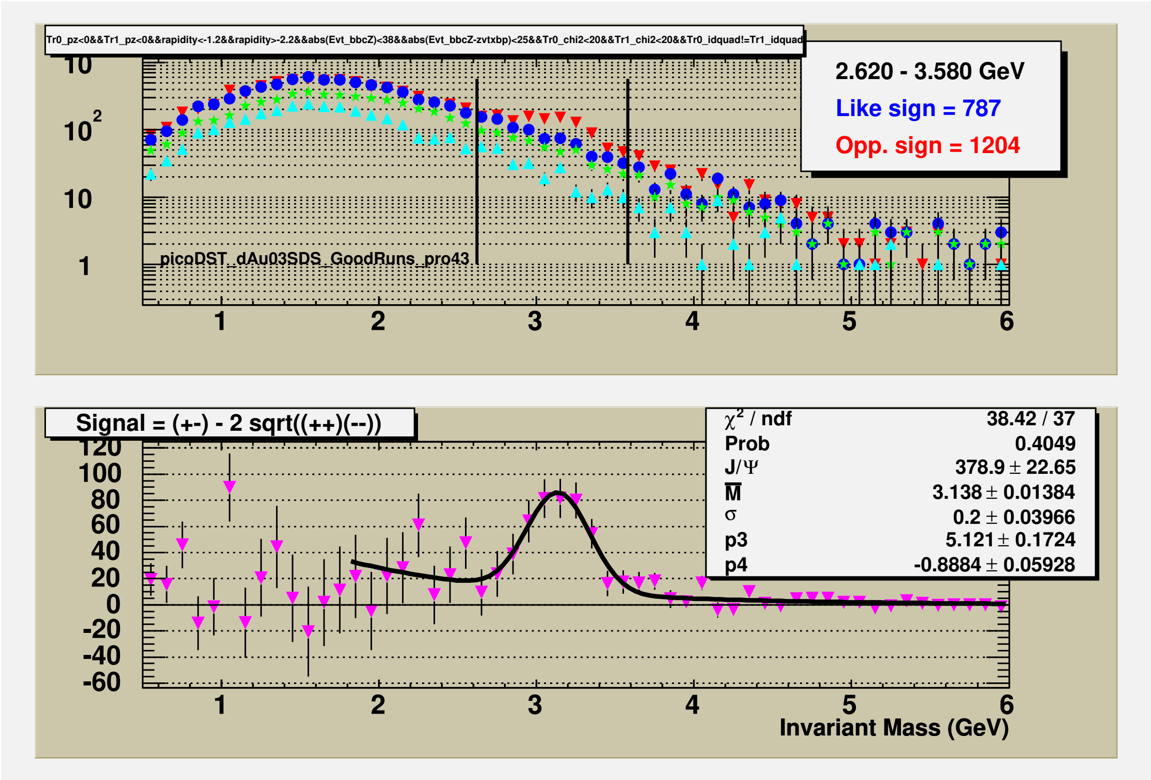


Figure 8: Invariant dimuon mass distributions for deuteron+gold data in the south arm (1D1S triggers).

The vertex range as used in AN210 is ±18 cm and no vertex dependence was found. At the time of this analysis, the BBC centrality was extended to the range ±40 cm and is consistent with the ±38 cm range used here.

For the neutron-tagged sample (the proton undergoes collisions with the Au nucleus), the average trigger efficiency is 16.8%. The same selection criteria for neutron-tagged events as used in AN210 are also used here (namely, requiring at least an energy of 60 GeV in the North ZDC).

A Monte Carlo Glauber model calculation that includes the BBC response was used in AN210 to determine the number of collisions for the centrality selections. These values are summarized in Table 13 for completeness.

In order to compare to theory, this same Glauber MC code is used to determine the $N_{coll}$ for a given impact parameter range. For the ranges used in our centrality comparison to theory, these values are in Table 14. It should be noted that DataThief was used to determine the equivalent values of Rda for the north arm comparison to theory.

## 6.1 Systematic Errors

Most of the systematic errors will be summarized in section 8. We only address here the ones which are specific to the centrality analysis.

### 6.1.1 Point-to-point

The point-to-point systematic errors include those errors in both Rcp and Rda that vary in a correlated way to $\langle N_{coll} \rangle$. The BBC bias (see table 12) and the $N_{coll}$ errors (see table 13) are the ones to be considered has point-to-point.

| system | arm | 1. e+g | 2. e+g | 3. q+g | 4. e+2g | 5. 2e+2g | 6. gaus | 7. e+g | error |
|---|---|---|---|---|---|---|---|---|---|
| dAu | N | 784(32) | 772(32) | 742(31) | 766(31) | 828(32) | 925(31) | 928(31) | 10.34% |
| dAu | S | 578(27) | 559(28) | 522(27) | 565(33) | 553(27) | 697(27) | 710(27) | 11.88% |
| pp | N | 290(19) | 270(19) | 286(13) | 292(19) | 292(19) | 326(18) | 332(18) | 7.12% |
| pp | S | 118(12) | 115(13) | 109(13) | 111(12) | 111(12) | 128(11) | 132(12) | 4.69% |
| dAu/pp | S | 4.88 | 4.87 | 4.78 | 5.10 | 4.99 | 5.45 | 5.40 | 3.7% |
| dAu/pp | N | 2.70 | 2.86 | 2.60 | 2.62 | 2.83 | 2.83 | 2.79 | 2.8% |

Table 11: Systematic uncertainties associated with the shapes and background descriptions used for fitting the mass spectra and extracting the $J/\psi$ yields. The last column is the systematic errors derive from this comparison.

| Centrality bin | Value | Error |
|---|---|---|
| 0-20 | 1.000 | 0.0008 |
| 20-40 | 0.995 | 0.003 |
| 40-60 | 0.974 | 0.01 |
| 60-88 | 0.885 | 0.04 |

Table 12: BBC centrality bias correction factor table.

#### 6.1.2 Systematic Errors in the Normalization

The errors that are independent of $\langle N_{coll}\rangle$ are considered separately. The only centrality-related uncertainty to be considered as global is when we derive the minimum bias Rda. We then need $\langle N_{coll}^{MB}\rangle$. Table 13 tells us that this error is 0.7/8.4 = 8.3%.

## 7 Cross Section Input Variables

We give below all the input variable used for the final cross section calculations.

### 7.1 $N_{J/\psi}$

This quantity is simply the number of identified $J/\psi$s derived by the real data analysis. The analysis cuts and the fitting procedure was described in previous sections (3.8 and 5).

### 7.2 $A \times \varepsilon_{J/\psi}^{4\pi}$

$A \times \varepsilon_{J/\psi}^{4\pi}$ is the product of the acceptance and efficiency for the muon arms (triggering and reconstruction) as given by realistic detector simulations. It is calculated for each bin by counting the number of $J/\psi$'s which are reconstructed, pass a simulated dimuon trigger, and pass the same cuts as were used in the real data selection, and dividing this by the number of $J/\psi$s generated in this same bin. Both numerator and denominator

include a cut on the vertex being within 38 cm of z=0. The resulting efficiencies can be found in tables 15 and 16 for each bin of interest.

The systematic errors from this section and sections 3.3 and 3.4 are summarized in table 19 and in the next section.

| Centrality bin | $\langle N_{coll}\rangle$ | Systematic Error | $\langle N_{coll}\rangle/\langle N_{coll}^{60-88}\rangle$ | Systematic Error |
|---|---|---|---|---|
| 0-20 | 15.0±1.0 | 6.6% | 4.6±0.5 | 10.2% |
| 20-40 | 10.4±0.7 | 6.9% | 3.2±0.2 | 7.7% |
| 40-60 | 6.9±0.6 | 8.5% | 2.1±0.1 | 4.0% |
| 60-88 | 3.2±0.3 | 9.7% | 1.0±0.0 | 0.0% |
| Min Bias (K. Reygers, AN216) | 8.4±0.7 | (included) | – | – |

Table 13: The $N_{coll}$ and errors as determined using Glauber MC and the BBC response (from AN210). The value used for Min Bias is taken from the note that synthesizes the various approaches, AN216, where the error includes both statistical and systematic uncertainties. The column showing the ratio of each centrality bin to the most peripheral is relevant for Rcp.

| Impact Parameter | $N_{coll}$ |
|---|---|
| $0.2 < b/R$ | 16.9 |
| $0.9 < b/R < 1.1$ | 3.5 |
| $1.9 < b/R < 2.1$ | 1.3 |

Table 14: The $N_{coll}$ using the MC Glauber calculation for a given impact parameter range (ranges as used in the paper by Klein and Vogt [15]).

### 7.3 $B_{\mu\mu}$

The particle data book lists the branching ratio for $J/\psi \to \mu^+\mu^-$ as $B_{\mu\mu} = 0.0588 \pm 0.0010$ [10]. We assign no systematic error due to this number.

### 7.4 $N_{MB}$

This is the number, integrated over all selected runs, of minimum-bias triggered events, included in the analysis. The luminosity numbers, calculated from the number of sampled events, for the different run periods, were given already in table 9.

**Systematic errors**

The number of background events, such as beam gas and beam scraping, was estimated to be small.

### 7.5 $\sigma_{tot}$

The total $dAu$ cross section at $\sqrt{s} = 200\,\mathrm{GeV}$ has not actually been measured. The HIJING value for the inelastic cross-section ($\sigma_{inel} = 2.25 \pm 0.1\,\mathrm{b}$), with a modified description of the deuteron by B. Cole and S. Johnson. Some description of this and a Glauber calc. for dAu can be found in [11]. The 'PHENIX standard' Glauber calc. result is 2.18 ± 0.08 b [12]. This is the value used in the calculation of $\varepsilon_{BBC}^{MB}$ and $\varepsilon_{BBC}^{J/\psi}$ in the next two sections. See the next section for a description of the error on this quantity. The total $pp$ cross section, based on an average of the available world data, is 42.2 ± 1.9 mb% [14].

The estimated systematic error is thus about 4.5% for each of these numbers.

### 7.6 $\varepsilon_{BBC}^{J/\psi}$

$\varepsilon_{BBC}^{J/\psi}$ is the BBC trigger efficiency for $J/\psi$ events which have a vertex that falls within a $|z| < 30$ cm. This was calculated by Monte Carlo simulations, and cross-checked with real data for the Run 2 pp analysis, and found to be 0.74 ± 0.01 (stat. only). Within systematic errors, a good agreement between the values for $J/\psi$'s in the central and muon arms, as well as for high $p_T$ pions in the central arms were found. This lead to the suggestion that the BBC trigger efficiency for hard processes could be process independent [7].

| Beam | Arm | Bin | Thrown | Reconstructed | 1D1S | 2D | $\varepsilon_{perfect}$ | $\varepsilon_{\mu\mu}$ | $\varepsilon_{1D1S}$ | $\varepsilon_{2D}$ |
|---|---|---|---|---|---|---|---|---|---|---|
| pp | S | All | 111841 | 4680 | 3069 | 0 | 0.128 | 0.327 | 0.656 | 0 |
| pp | S | y1 | 49193 | 2356 | 1553 | 0 | 0.128 | 0.374 | 0.659 | 0 |
| pp | S | y2 | 62648 | 2324 | 1516 | 0 | 0.128 | 0.290 | 0.652 | 0 |
| pp | N | All | 126387 | 10498 | 9049 | 0 | 0.127 | 0.654 | 0.862 | 0 |
| pp | N | y1 | 73890 | 6036 | 5215 | 0 | 0.127 | 0.643 | 0.864 | 0 |
| pp | N | y2 | 52497 | 4462 | 3834 | 0 | 0.127 | 0.669 | 0.859 | 0 |
| dAu | S | All | 111841 | 6951 | 5654 | 3489 | 0.128 | 0.486 | 0.813 | 0.502 |
| dAu | S | y1 | 49193 | 3274 | 2688 | 1667 | 0.128 | 0.520 | 0.821 | 0.509 |
| dAu | S | y2 | 62648 | 3677 | 2966 | 1822 | 0.128 | 0.459 | 0.807 | 0.496 |
| dAu | N | All | 126387 | 10779 | 9262 | 6781 | 0.127 | 0.672 | 0.859 | 0.629 |
| dAu | N | y1 | 73890 | 6082 | 5234 | 3753 | 0.127 | 0.648 | 0.861 | 0.617 |
| dAu | N | y2 | 52497 | 4697 | 4028 | 3028 | 0.127 | 0.705 | 0.858 | 0.645 |

Table 15: Summary of the simulation results used to obtain the $J/\psi$ efficiency for each bin in rapidity. For the South arm All is $-2.2 < y < -1.2$, y1 is $-2-2 < y < -1.7$, and y2 is $-1.7 < y < -1.2$. While for the North arm All is $1.2 < y < 2.4$, y1 is $1.2 < y < 1.8$, and y2 is $1.8 < y < 2.4$. 2D is the two-deep road trigger, while 1D1S is the one-deep and one-shallow road trigger.

For the dAu high $p_T$ result, this bias was described and estimated in [8] and [9]. We assume that the process independence holds, and use these numbers for this note, that is 0.92. For the centrality analysis (see section 6), we correct for the numbers quoted in table 12.

As stated in Hiroki Sato's thesis [7] the BBC efficiency does not have any significant $z_{vtx}$ dependence in the $\pm 38cm$ range. So we assume it's efficiency remains the same for $\pm 38$ cm as for $\pm 30$ cm. One can also see in AN211 [13] that there is no significant effect found in comparisons of $\pm 30$ cm to $\pm 20$ cm.

### 7.7 $\varepsilon_{BBC}^{MB}$

$\varepsilon_{BBC}^{MB}$ is the fraction of inelastic collisions that occur within X cm of $z = 0$ which will fire the minimum bias trigger (BBLL1($>1$)) and which have their offline BBC $|z_{vtx}|$ reconstructed within 30 cm of $z = 0$. $\varepsilon_{BBC}^{MB}$ was estimated to be about 0.885 for dAu [9] using a parametrization of BBC response, and $0.88 \pm 0.04$ from simulations [13] and other studies. The *pp* cross section, as seen by the BBC has been measured, and found to be 21.8 mb $\pm$ 9.6% [14], and the eff. of the BBC found to be 0.516 $\pm$ 9.8% [14].

Some uncertainties regarding these numbers should cancel in the ratio dAu over pp, but at the moment of writing it is not clear exactly how much. So, for now, we'll be conservative and just add all the errors in quadrature.

# 8 Summary of systematic errors

## 8.1 Analysis related systematics

- **Tube efficiency (including BLT)** - using the difference between random benefit corrected and non-random benefit corrected tube efficiencies, an average difference in tube efficiencies of approximately 0.5% gives approximately a 3% difference in $J/\psi$ efficiency results. For the tube efficiencies, Sean estimates a systematic of $-1.5\%$ and $+1\%$. This then scales to about $-9\%$ and $+6\%$ in the $J/\psi$ efficiency. For the ratio we assume that part of this cancels and use 1/2 this amount as shown in table 17.

- **Muon tracker efficiency** - The disagreement discussed in the muon tracking efficiency section earlier is close to being resolved, but questions still remain. So we will assign 1/2 of the original difference for pairs (13% for the south arm and 19% for the north arm) as a systematic error on the cross sections.

| Beam | Arm | Bin | Thrown | Reconstructed | 1D1S | 2D | $\varepsilon_{perfect}$ | $\varepsilon_{\mu\mu}$ | $\varepsilon_{1D1S}$ | $\varepsilon_{2D}$ |
|---|---|---|---|---|---|---|---|---|---|---|
| pp | S | pt1 | 32310 | 1440 | 948 | 0 | 0.128 | 0.348 | 0.658 | 0 |
| pp | S | pt2 | 52146 | 2161 | 1414 | 0 | 0.128 | 0.324 | 0.654 | 0 |
| pp | S | pt3 | 22370 | 838 | 552 | 0 | 0.128 | 0.293 | 0.659 | 0 |
| pp | S | pt4 | 4347 | 200 | 128 | 0 | 0.128 | 0.359 | 0.640 | 0 |
| pp | S | pt5 | 555 | 33 | 20 | 0 | 0.128 | 0.465 | 0.606 | 0 |
| | | | | | | | | | | |
| pp | N | pt1 | 36557 | 3136 | 2697 | 0 | 0.127 | 0.675 | 0.860 | 0 |
| pp | N | pt2 | 59235 | 4927 | 4248 | 0 | 0.127 | 0.655 | 0.862 | 0 |
| pp | N | pt3 | 25303 | 1974 | 1717 | 0 | 0.127 | 0.614 | 0.870 | 0 |
| pp | N | pt4 | 4622 | 407 | 343 | 0 | 0.127 | 0.693 | 0.843 | 0 |
| pp | N | pt4 | 569 | 45 | 35 | 0 | 0.127 | 0.623 | 0.778 | 0 |
| dAu | S | pt1 | 32310 | 2130 | 1718 | 1169 | 0.128 | 0.515 | 0.807 | 0.549 |
| dAu | S | pt2 | 52146 | 3252 | 2639 | 1788 | 0.128 | 0.487 | 0.812 | 0.550 |
| dAu | S | pt3 | 22370 | 1231 | 1009 | 692 | 0.128 | 0.430 | 0.820 | 0.562 |
| dAu | S | pt4 | 4347 | 281 | 241 | 171 | 0.128 | 0.505 | 0.858 | 0.609 |
| dAu | S | pt5 | 555 | 48 | 41 | 31 | 0.128 | 0.676 | 0.854 | 0.646 |
| dAu | N | pt1 | 36557 | 3244 | 2776 | 2193 | 0.127 | 0.699 | 0.856 | 0.676 |
| dAu | N | pt2 | 59235 | 5073 | 4364 | 3432 | 0.127 | 0.674 | 0.860 | 0.677 |
| dAu | N | pt3 | 25303 | 1984 | 1726 | 1369 | 0.127 | 0.617 | 0.870 | 0.690 |
| dAu | N | pt4 | 4622 | 417 | 349 | 291 | 0.127 | 0.710 | 0.837 | 0.698 |
| dAu | N | pt5 | 569 | 51 | 39 | 31 | 0.127 | 0.706 | 0.765 | 0.608 |

Table 16: Summary of the simulation results used to obtain the $J/\psi$ efficiency for each bin in $p_T$. The bins are $0 < p_T < 1$ (pt1), $1 < p_T < 2$ (pt2), $2 < p_T < 3$ (pt3), $3 < pT < 4$ (pt4), and $4 < p_T < 5$ (pt5). 2D is the two-deep road trigger, while 1D1S is the one-deep and one-shallow road trigger.

This systematic will go only in the direction of larger cross section since this is the direction of the original disagreement. Although one might expect this systematic to be the same for pp and dAu if it comes from the tracker, that is not proven. However, Nicki did indicate that the problem had similar magnitude for pp and dAu. Nevertheless, we will include 1/4 of the original disagreement for the ratios of dAu/pp.

- **Attenuated strips** - The effect of north attenuated strips on efficiency is obtained from simulations. *It is possible that this is related to the above, so this might be an overestimate.* We take an asymmetric systematic of 5% towards larger cross section (for north only) and assume this probably cancels in a ratio of dAu/pp.
- **Fitting method** - Uncertainty due to model dependence of fitting functions and procedures. See fitting dimuon spectra section and table 11.
- **Double counting (ghosts)** - The number of events with more than one dimuon contributing to the $J/\psi$ mass region has been counted (see table 18). They should be ghosts. For now we keep them but assign a 1.5% asymmetric systematic towards smaller cross section and smaller ratio.
- **Combinatoric bkgd method** - We assign a 5% systematic uncertainty, as it was described in section 5.1.
- **Trigger Circuit Efficiency** - negligible (the correction itself is very small, 5% or less).
- **Event mixing/embedding** - So far, no statistically significant evidence for a net non-zero effect here. Present results are statistics limited at the 3% level, so we assign a 3% systematic (see table 10).

| beam or ratio | arm | systematic |
|---|---|---|
| pp | S | $-9, +6\%$ |
| | N | $-9, +6\%$ |
| dAu | S | $-9, +6\%$ |
| | N | $-9, +6\%$ |
| R(dAu/pp) | S | $-4.5, +3\%$ |
| | N | $-4.5, +3\%$ |

Table 17: Estimated systematic uncertainties associated with determination of the muon identification tube efficiencies.

| beam | arm | trigger | $\mu^{\pm}\mu^{\pm}$ | $\mu^{+}\mu^{-}$ |
|---|---|---|---|---|
| pp | S | 1d1s | 0 | 0 |
| | N | 1d1s | 1.3% | 0.3% |
| dAu | S | 1d1s | 0.8% | 1.5% |
| | S | 2d | 0.9% | 0.6% |
| | N | 1d1s | 0.3% | 0 |
| | N | 2d | 2.6% | 0.9% |

Table 18: Upper limits for different beams, arms and triggers on the number of possible ghost pairs contributing to the $J/\psi$ yield.

- **MuTr HV state variations** (run2 3%) - We assume the same as the run 2 analysis and what DongJo suggests - a systematic of 3%.
- **MC representation** - MC vrs data distributions - use same as run 2, 5%.
- **Rapidity distribution** - use same as run 2, 3%.

  A summary of all the systematic uncertainties is in Table 19.

### 8.2 Absolute normalization systematics summary

- Overall abs. norm systematics: pp 12%, dAu 6% (quadrature sum of below contributions). Summarized in table 21.
- $N_{MB}$ - bkgd events negligible (as in run2, see AN194)
- $\sigma_{tot}$ - pp 42.2(1.9) mb, AN184; dAu 2.81(0.08 ) b, Reygers priv. comm.
- $\varepsilon^{MB}_{BBC}$ - pp 0.516(9.8%) AN184; dAu 0.88(0.04) AN211
- In AN184, the product $\sigma_{tot} \times \varepsilon^{MB}_{BBC}$ is estimated to suffer a 9.6 % systematic errors.
- $\varepsilon^{J/\psi}_{BBC}$ - pp 0.74(5%) AN194; dAu 0.92(2%) AN209

  Nominally $\varepsilon^{MB}_{BBC}$ above are valid for $\pm 30$ cm, but as Hiroki says in his thesis these efficiencies are not significantly $z_{vtx}$ dependent in the range $\pm 38$ cm. Also from An211 the efficiencies for two $z_{vtx}$ ranges are equal within uncertainties. See Table 20.

## 9 Results Summary

In some of the figure we shox, we add points from the dielectron analysis [18].

| Systematic error | pp South | pp North | dAu South | dAu North | Ratio South | Ratio North |
|---|---|---|---|---|---|---|
| Fitting | ±7.1% | ±4.7% | ±10.3% | ±11.9% | ±3.7% | ±2.8% |
| Ghosts | −1.5% | −1.5% | −1.5% | −1.5% | −1.5% | −1.5% |
| Combinatorial Background | ±5% | ±5% | ±5% | ±5% | ±5% | ±5% |
| Point-to-point | +8.7% | +6.9% | +11.4% | +12.9% | +6.4% | +5.9% |
| | −8.8% | −7.0% | −11.5% | −13.0% | −6.4% | −5.9% |
| MuID Tube Efficiency | +6 − 9% | +6 − 9% | +6 − 9% | +6 − 9% | +3 − 6% | +3 − 6% |
| MuTr Chamber Efficiency | +6.5% | +9.5% | +6.5% | +9.5% | +3.3% | +4.8% |
| MuTr Attenuated Strips | 0.0% | ±5% | 0.0% | ±5% | 0.0% | ±5% |
| Event Mixing Error | ±3% | ±3% | ±3% | ±3% | ±3% | ±3% |
| MuTr HV state | ±3% | ±3% | ±3% | ±3% | ±3% | ±3% |
| Arm-to-Arm | +9.8% | +13.0% | +9.8% | +13.0% | +6.2% | +8.7% |
| | −9.9% | −11.1% | −9.9% | −11.1% | −8.1% | −10.1% |
| MuTr MC Represent. | ±5% | ±5% | ±5% | ±5% | 0.0% | 0.0% |
| Rapidity Distr. | ±3% | ±3% | ±3% | ±3% | 0.0% | 0.0% |
| Global | +5.8% | +5.8% | +5.8% | +5.8% | 0.0% | 0.0% |
| | −5.8% | −5.8% | −5.8% | −5.8% | 0.0% | 0.0% |
| SUM | +14.3% | +15.8% | +16.2% | +19.2% | +8.9% | +10.5% |
| | −14.5% | −14.4% | −16.3% | −18.1% | −10.3% | −11.7% |

Table 19: Summary of systematic errors. All errors listed are fractional errors in %. Top box are for errors to be applied independently to each point. In the middle box, are errors which depend on the arm we consider but should be the same for all points within this arm. The bottom box is for errors that are independent of any selection.

| $z_{vtx}$ | $N_{Tag}$ | $\pi^0$ | minBias |
|---|---|---|---|
| $\pm 20cm$ | 72.8% | 94.8% | 87.5% |
| $\pm 30cm$ | 73% | 94.8% | 87.2% |

Table 20: BBC efficiencies from AN211 which show negligible differences between vertex ranges of $\pm 30cm$ and $\pm 20cm$.

## 9.1 $J/\psi$ differential cross section versus rapidity

Figures 9, 10, show the differential cross sections versus rapidity for both pp and dAu, according to equation 1. All the relevant numbers are reported in table 22.

The rapidity distribution (including the dielectron points) was fitted to a Pythia shape and we found:

$$BR \times \sigma_{tot} = 159 \pm 13.5\, nb \pm 12.3\%(syst) \tag{3}$$

to be compared with the published run2 results of $234 \pm 36(stat) \pm 34(syst) \pm 24(abs)$ [19]. Assuming the uncertainties are independent, these two results are 1.3 sigma appart. The Pythia calculation used was one of the same ones used for the Run2 rapidity distributions fits discussed in [1] and used the GRV94HO structure functions. The first uncertainty quoted here is simply the statistical uncertainty from the fit. The global systematical error that applies to all the points also apply to $BR \times \sigma_{tot}$ and is 12.3 %. For the Run2 analysis, the variation for different rapidity model shapes form was found to be within 3% and we neglect it here.

| Beam | Arm | Quantity | Value | Uncertainty |
|---|---|---|---|---|
| pp | S | $N_{MB}$ | $4.50 \times 10^9$ | 0 |
| pp | N | $N_{MB}$ | $4.02 \times 10^9$ | 0 |
| pp | | $\varepsilon_{BBC}^{MB}$ | 0.516 | 9.8% |
| pp | | $\sigma_{pp}^{tot}$ | 42.2 mb | 1.9 mb |
| pp | | $\varepsilon_{BBC}^{MB} \times \sigma_{pp}^{tot}$ | | 9.6 % |
| pp | | $\varepsilon_{BBC}^{J/\psi}$ | 0.74 | 5% |
| total | | | | 10.8 % |
| global | | | + 5.8% = | 12.3 % |
| dAu | S | $N_{MB}$ | $2.70 \times 10^9$ | 0 |
| dAu | N | $N_{MB}$ | $3.31 \times 10^9$ | 0 |
| dAu | | $\varepsilon_{BBC}^{MB}$ | 0.88 | 0.04 |
| dAu | | $\sigma_{dAu}^{tot}$ | 2.18 b | 0.08 b |
| dAu | | $\varepsilon_{BBC}^{J/\psi}$ | 0.92 | 2% |
| total | | | | 6.2 % |
| global | | | + 5.8% = | 8.5 % |

Table 21: Summary of common normalization factors used in the cross section calculations and their systematic uncertainties. "total" stands for the quadratic sum of these errors, while global add the other "global" uncertainties from table 19.

### 9.2 $J/\psi$ differential cross section versus transverse momentum

Figures 11 and 12 show the differential cross sections versus transverse momentum for both pp and dAu, according to equation 1. All the relevant numbers are reported in table 23.

The transverse momentum shapes were fitted to $A \times (1 + (p_T/B)^2)^{-6}$ and found to be:

- $3.77 \times (1 + (p_T/3.29)^2)^{-6}$ for pp
- $833 \times (1 + (p_T/4.23)^2)^{-6}$ for dAu South
- $638 \times (1 + (p_T/4.00)^2)^{-6}$ for dAu North

The average $< p_T^2 >$ values ($B^2/4$) from these fits are :

- $2.70 \pm 0.24$ for pp
- $4.47 \pm 0.25$ for dAu South
- $3.99 \pm 0.25$ for dAu North

which give $\Delta < p_T^2 >$ values for the difference between dAu and pp of :

- $1.77 \pm 0.35$ for dAu South
- $1.29 \pm 0.35$ for dAu North

We define $C$ to be $\Delta < pT^2 >= C \times [(A/2)^{1/3} - 1]$ and plot it versus $\sqrt{s}$ together with lower energy experiments in figure 13. A simple linear fit including the lower energy $J/\psi$ results gives :

$$C = 0.0297 + 0.002226 \times \sqrt{s} \quad (4)$$

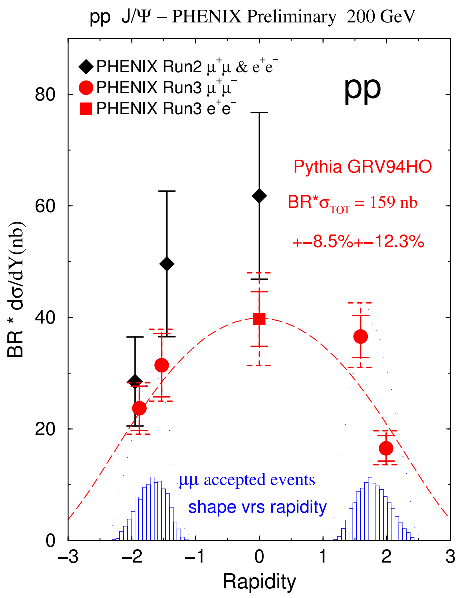


Figure 9: Differential cross section for pp versus rapidity. Solid error bars represent statistical + point-to-point systematics and the dashed error bars include arm-to-arm errors. A global 12.3 % error bar is not displayed (see tables 19 and 21).

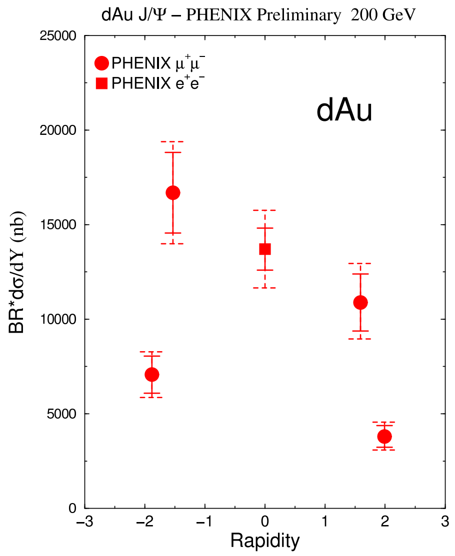


Figure 10: Differential cross section for dAu versus rapidity. Solid error bars represent statistical + point-to-point systematics and the dashed error bars include arm-to-arm errors. A global 8.5% error bar is not displayed (see tables 19 and 21).

## 9.3 Comparing dAu to pp. Shadowing.

Figure 14 shows the ratio $R_{dAu}$ of the per nucleon cross section for dAu to that for pp, i.e. :

$$R_{dAu} = \frac{\sigma_{dAu}}{2 \times 197 \times \sigma_{pp}} \tag{5}$$

Figures 15, 16, and 17 show the value of alpha versus rapidity, $x_F$ and $x_2$, compared to the lower energy fixed target experiments E866/NuSea at $\sqrt{s} = 38$ GeV [16] and NA3 at $\sqrt{s} = 19$ GeV [17]. Alpha is defined as follow :

$$\sigma_{dAu} = \sigma_{pp} \times (2 \times 197)^{\alpha} \tag{6}$$

## 9.4 $\alpha$ dependence on $p_T$

Figure 18 shows alpha versus transverse momentum.

## 9.5 Centrality dependence

Figure 20 shows the ratio of the dAu cross sections between more central and the most peripheral centrality bin, while 19 shows the dependence on centrality of the dAu/pp ratio.

Our dAu/pp ratio is computed from the quantities reported in table 24 with Equation 7:

$$\mathcal{R}(N_{coll}) = \frac{d\sigma^{J/\psi}_{dAu}/dY}{AB \times d\sigma^{J\psi}_{pp}/dY} / \frac{N_{coll} \times width}{N^{MB}_{coll} \times \sum width} \tag{7}$$

where

1. $AB = (2)(197)$ is the total number of nucleons in the dAu collision system,
2. $N^{MB}_{coll}$ is the number of collisions in minimum bias events $8.4 \pm 0.7$ from table 13,

| $Y$ | $\#J/\psi$ | $\epsilon_{perfect}$ | $\epsilon_{\mu\mu}$ | $\epsilon_{BLT}$ | $\epsilon_{TCE}$ | $L$ ($nb^{-1}$) | $\epsilon_{BBC}^{J/\psi}$ | $BR * d\sigma_{J/\psi}$ ($nb$) | $R_{dAu}$ | $\alpha$ |
|---|---|---|---|---|---|---|---|---|---|---|
| dAu: | | | | | | | | | | |
| -1.71 | 578(27) | 0.128 | 0.486 | 0.679 | 0.99 | 1.43 | 0.92 | 10479(512) | 0.998(092) | 1.000(015) |
| -1.88 | 211(16) | 0.128 | 0.52 | 0.687 | 0.99 | 1.43 | 0.92 | 7072(555) | 0.923(140) | 0.987(025) |
| -1.53 | 431(23) | 0.128 | 0.459 | 0.673 | 0.99 | 1.43 | 0.92 | 16695(947) | 1.190(126) | 1.029(018) |
| 1.76 | 784(31) | 0.127 | 0.672 | 0.750 | 0.93 | 1.70 | 0.92 | 7016(289) | 0.668(059) | 0.933(015) |
| 1.59 | 583(27) | 0.127 | 0.648 | 0.745 | 0.93 | 1.70 | 0.92 | 10888(529) | 0.776(079) | 0.958(017) |
| 1.99 | 225(17) | 0.127 | 0.705 | 0.757 | 0.93 | 1.70 | 0.92 | 3802(295) | 0.496(075) | 0.883(025) |
| pp: | | | | | | | | | | |
| -1.71 | 118(12) | 0.128 | 0.327 | 0.656 | 0.99 | 208 | 0.74 | 28.192(2.913) | | |
| -1.88 | 57(8) | 0.128 | 0.374 | 0.659 | 0.99 | 208 | 0.74 | 23.705(3.383) | | |
| -1.53 | 58(9) | 0.128 | 0.29 | 0.652 | 0.99 | 208 | 0.74 | 31.442(4.947) | | |
| 1.76 | 290(19) | 0.127 | 0.654 | 0.862 | 0.95 | 185 | 0.74 | 26.002(1.725) | | |
| 1.59 | 201(15) | 0.127 | 0.643 | 0.864 | 0.95 | 185 | 0.74 | 36.575(2.776) | | |
| 1.99 | 94(11) | 0.127 | 0.669 | 0.859 | 0.95 | 185 | 0.74 | 16.536(1.954) | | |
| pp avg: | | | | | | | | | | |
| 1.74 | | | | | | | | 26.641(2.072) | | |
| 1.56 | | | | | | | | 35.606(3.186) | | |
| 1.94 | | | | | | | | 19.452(2.535) | | |

Table 22: Calculation of the cross sections and ratios versus rapidity for the two muon arms. The pp average cross section used to form the ratios assuming symmetry around y=0 is shown at the bottom (where the rapidity value listed is the average absolute value). The quantities in the third and fourth columns are from table 15, $\varepsilon_{BLT}$ is the luminosity weighted average of the 1D1S and 2D trigger efficiencies, and $L = N_{MB}/(\sigma_{tot} \times \varepsilon_{BBC}^{MB})$ is the total luminosity for both triggers.

3. $\Sigma$width = 0.88 is the total sum of the centrality bin widths, while *width* is the width of the centrality bin (0.20 or 0.28). This is to normalized to the correct partial luminosity.

4. The $d\sigma_{dAu}^{J/\psi}/dY$ computation is done as in equation 1, the ratio of BBC efficiencies being the *bias* number from table 12.

Again, this is not the usual PHENIX standard, but it can simply be obtained by $R_{dAu} = (0.91 \pm 0.09)\mathcal{R}$. The right axis stands for it on figure 19.

The Rcp is also tabulated and is determined using Equation 8,

$$R_{cp} = \frac{N_{J/\psi}/N_{coll}}{N_{J/\psi}^{60-88\%}/N_{coll}^{60-88\%}} \tag{8}$$

# 10 Some cross-checks

## 10.1 Vertex cut

Because we used different vertex cuts to compute the number of events $N_{J/\psi}$ and $N_{MB}$ ($\pm 38$ cm) and to correct for the bbc efficiency $\varepsilon_{BBC}^{J/\psi}$ and $\varepsilon_{BBC}^{MB}$ ($\pm 30$ cm) we made a full consistency check of the differences between the two cuts. First, let us remind that the analysis/normalization procedure used is:

- Calculate Acc$\times$Eff from simulation using a vertex distribution thrown with sigma=39cm but cut at $\pm 38$ cm, and reconstructed consistently.

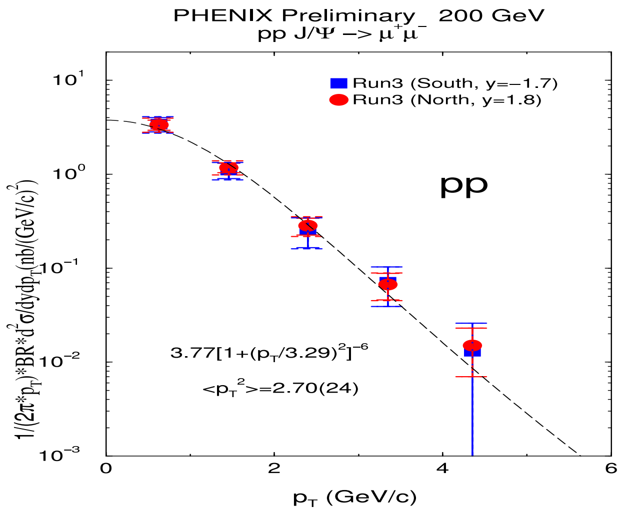


Figure 11: Invariant cross section for pp versus transverse momentum. Solid error bars represent statistical + point-to-point systematics and the dashed error bars include arm-to-arm errors. A global 12.3 % error bar is not displayed (see tables 19 and 21). Results from the 2002 run are shown in black for comparison.

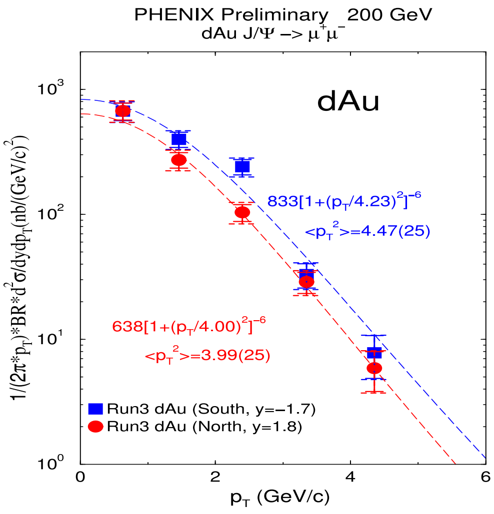


Figure 12: Invariant cross section for dAu versus transverse momentum. Solid error bars represent statistical + point-to-point systematics and the dashed error bars include arm-to-arm errors. A global 8.5 % error bar is not displayed (see tables 19 and 21).

- Count the $J/\psi$'s in the data with a $\pm38$ cm zvtx cut.
- Count the BBCLL1 luminosity with a $\pm38$ cm zvtx cut.
- Use $\varepsilon_{BBC}$ and $\varepsilon_{BBC}^{J/\psi}$ from $\pm30$ cm and assume no change in their relative values for $\pm38$ cm.

Then let's see how things move if we try both vertex cuts consistently on each part:

1. The fraction of $J/\psi$'s that pass each cut ($\pm30/\pm38$ cm) is :
   - In pp, $116/118 = 0.98$ for the south and $279/290 = 0.96$ for the north.
   - In dAu, $526/578 = 0.91$ for the south and $695/784 = 0.89$ for the north.

   Thus, about 3% (pp) and 10% (dAu) of the $J/\psi$'s are lost if we were to analyze with a $\pm30$ cm cut instead of our $\pm38$ cm.

2. On the other hand, the fraction of BBCLL1 luminosity lost is :
   - In pp, 98% for $\pm38$ cm, 93% for $\pm30$ cm, thus 96% for the ($\pm30/\pm38$ cm) ratio.
   - In dAu 1D1S, 92% for $\pm38$ cm, 82% for $\pm30$ cm, thus 89% for the ($\pm30/\pm38$ cm) ratio.
   - In dAu 2D, 96% for $\pm38$ cm, 86% for $\pm30$ cm, thus 89% for the ($\pm30/\pm38$ cm) ratio.

   Thus, the loss in luminosity for the change in vertex cut is about $\sim 4\%$ for pp and $\sim 11\%$ for dAu. Identical to the loss of J/Psi counts above, within statistics. This of course implies that the results will not change (except to give lower statistics) if we were to do everything for $\pm30$ cm.

3. The change in $J/\psi$ efficiency between $\pm38$ and $\pm30$ cm vertex cuts :
   - The BLT efficiency goes from 65.6% to 65.6% in the south, and from 86.2% to 86.1% in the south.
   - The dimuon reconstruction efficiency goes from 32.7% to 33.1% in the south (37.4%/37.8% and 29.0%/29.4% in our two rapidity bins) and from 65.4% to 66.0% in the north (64.3%/64.7% and 66.9%66.9%).

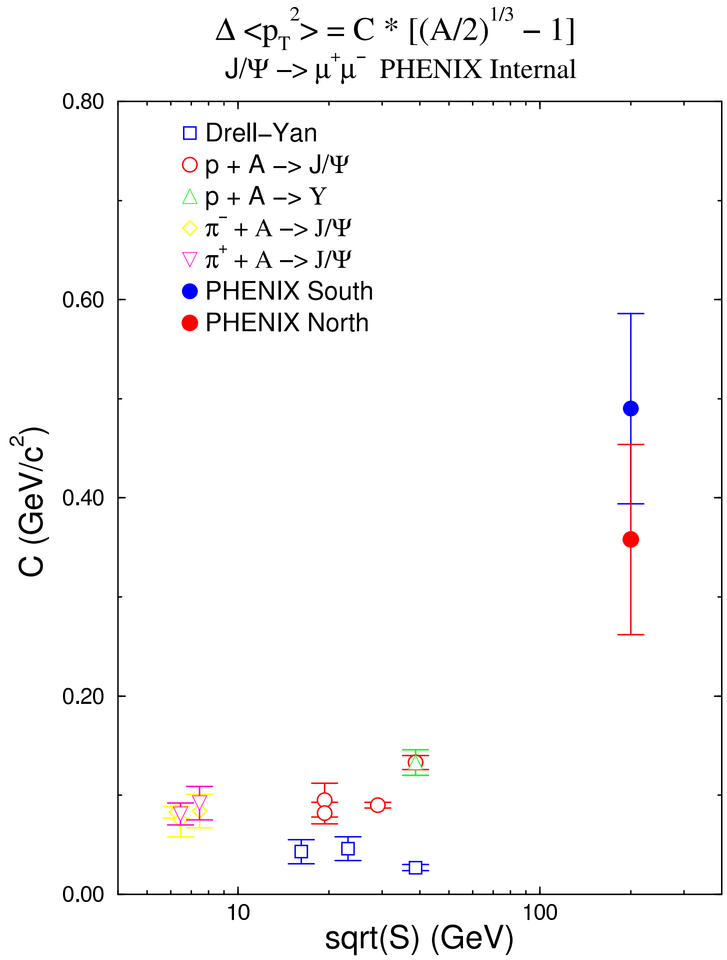


Figure 13: The C factor as defined at the top of the plot versus $\sqrt{s}$.

So the worst statistics above is about 2.7% from the number of accepted simulated counts, While the worst differences are 1.3% in the south and 0.9% in the north. So there is no change within the simulation statistics.

4. Some comments on the BBC efficiency:
   - From Hiroki Sato's thesis [7], p. 163, "no z-vertex dependence within $|zvtx| < 38$ cm is actually found over the statistical uncertainty of the simulation study ($< 3\%$)"
   - Also from analysis note AN211 (see table 20) there is no significant dependence in BBC efficiency for NTag, $\pi^0$, or min-bias between $\pm 30$ cm and $\pm 20$ cm. This *suggests* that one would also not see much, if any, dependence between $\pm 30$ cm and $\pm 38$ cm.
   - Note also that we're only sensitive to differences in the $\varepsilon_{BBC}^{J/\psi}$ and $\varepsilon_{MB}$ ratio.

5. On the width of the zvtx distribution in simulations and whether it matches the real vertex distribution: About 17% of simulated $J/\psi$'s *thrown* in zvtx rms 39 cm are lost when one changes the zvtx cut from 38 to 30 cm. This is clearly more than seen for real data (4% pp, 10% dAu) and must reflect the difference between the BBCLL1 zvtx calculation and the one offline. But given there is no change in $J/\psi$ efficiency between 30 and 38 cm this should not affect our results.

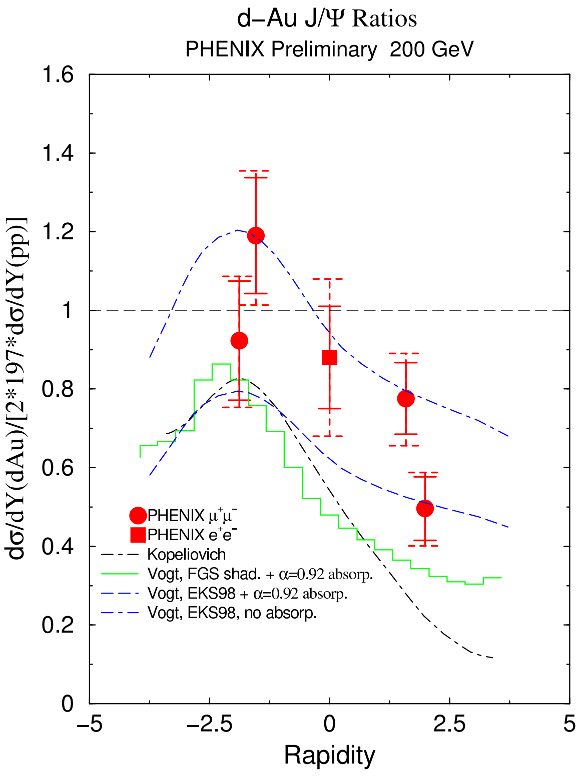


Figure 14: Ratio of per nucleon cross sections of dAu to pp versus rapidity. Solid error bars represent statistical + point-to-point systematics and the dashed error bars include arm-to-arm errors. A global 13.4 % error bar is not displayed (see tables 19 and 21).

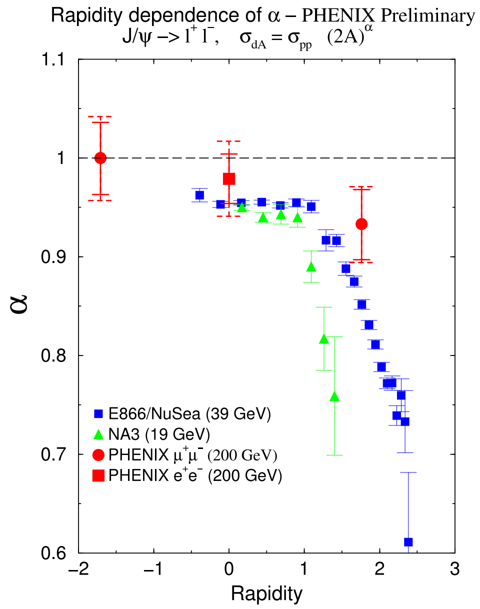


Figure 15: Alpha versus rapidity. Solid error bars represent statistical + point-to-point + arm-to-arm systematics, while the dashed error bars include the global uncertainty (see tables 19 and 21). Results from the E866/NuSea and NA3 fixed target experiments at lower energy ($\sqrt{s}$ = 38 GeV and 19 GeV) are shown for comparison.

### 10.2 Trigger subsets compared to total

Some inconsistancy was observed in the $J/\psi \to e^+e^-$ analysis in RdA versus centrality, when they divide the data into two different trigger configurations. Their change occurs at the same time we change our trigger configuration, that is when we changed from one-deep and one-shallow (1D1S) to two-deep (2D) muon triggers. As a cross check, we compute RdA independently for these two different data sets taken at different times with these two different trigger configurations.

In Table 25, the entire data sample is divided into the two respective trigger types: deep-deep triggers (2D) and deep-shallow triggers (1D1S). The difference of these two independent subsamples is shown in the 2D−1D1S column. Apart from the 20-40 centrality bin in the South muon arm, where a bad fit to the mass spectrum ("BF") invalidates the comparison, the two samples seem in fair agreement.

It is also useful to point out that not only do these triggered subsets agree in Rcp, they also agree in other quantities of interest; such as the cross section versus rapidity, where we also made a similar comparison.

## References


[1] PHENIX Analysis Note 194.

[2] PHENIX Analysis Note 163.

[3] PHENIX Technical Note 395.

[4] http://www.phenix.bnl.gov/phenix/WWW/p/draft/djkim/run3pp/

[5] http://www.phenix.bnl.gov/phenix/WWW/p/draft/silvermy/dAu/

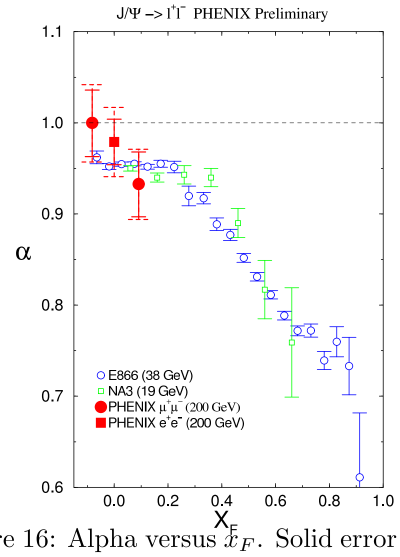


Figure 16: Alpha versus $x_F$. Solid error bars represent statistical + point-to-point + arm-to-arm systematics, while the dashed error bars include the global uncertainty (see tables 19 and 21). Results from the E866/NuSea and NA3 fixed target experiments at lower energy ($\sqrt{s}$ = 38 GeV and 19 GeV) are shown for comparison.

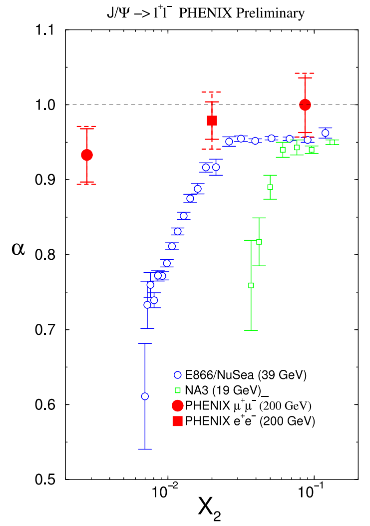


Figure 17: Alpha versus $x_2$. Solid error bars represent statistical + point-to-point + arm-to-arm systematics, while the dashed error bars include the global uncertainty (see tables 19 and 21). Results from the E866/NuSea and NA3 fixed target experiments at lower energy ($\sqrt{s}$ = 38 GeV and 19 GeV) are shown for comparison.


[6] MUID software description reference

[7] H. D. Sato, Kyoto Univ., (PHENIX) Thesis.

[8] PHENIX Analysis Note 209.

[9] PHENIX Analysis Note 210.

[10] http://pdg.lbl.gov/2002/m070.pdf

[11] PHENIX Analysis Note 216.

[12] K. Reygers, private communication.

[13] PHENIX Analysis Note 211.

[14] PHENIX Analysis Note 184.

[15] NUCL-TH/0305046.S.R.Klein, R.Vogt, PRL 91, 142301 (2003).

[16] E866/NuSea: M.J. Leitch et al, PRL 84, 3256 (2000)

[17] NA3: J.Badier et al Z. Phys. C20, 101 (1983)

[18] PHENIX Analysis Note 258. Xie Wei. $J/\psi \rightarrow e^+e^-$ analysis in RUN3 d-Au and RUN3 p-p for QM04.

[19] hep-ex/0307019. PHENIX. $J/\psi$ production from proton-proton collisions at sqrt(s) = 200 GeV.

| $p_T$ | $\#J/\psi$ | $\epsilon_{perf}$ | $\epsilon_{\mu\mu}$ | $\epsilon_{BLT}$ | $\epsilon_{TCE}$ | $L$ $(nb^{-1})$ | $\epsilon_{BBC}^{J/\psi}$ | $BR \times d\sigma_{J/\psi}$ $(nb)$ | RdA | $\alpha$ |
|---|---|---|---|---|---|---|---|---|---|---|
| dAu: | South | | | | | | | | | |
| 0.63 | 126(14) | 0.128 | 0.515 | 0.696 | 0.99 | 1.43 | 0.92 | 669(76) | 0.504(082) | 0.885(027) |
| 1.46 | 214(16) | 0.128 | 0.487 | 0.699 | 0.99 | 1.43 | 0.92 | 399(31) | 0.874(121) | 0.978(023) |
| 2.40 | 193(14) | 0.128 | 0.43 | 0.709 | 0.99 | 1.43 | 0.92 | 241.2(19.3) | 2.220(531) | 1.133(040) |
| 3.35 | 46(8) | 0.128 | 0.505 | 0.75 | 0.99 | 1.43 | 0.92 | 33.05(6.19) | 1.230(483) | 1.035(066) |
| 4.35 | 19(6) | 0.128 | 0.676 | 0.764 | 0.99 | 1.43 | 0.92 | 7.786(2.778) | 1.376(986) | 1.053(120) |
| dAu: | North | | | | | | | | | |
| 0.63 | 253(21) | 0.127 | 0.699 | 0.77 | 0.93 | 1.70 | 0.92 | 674(58) | 0.507(073) | 0.886(024) |
| 1.46 | 297(18) | 0.127 | 0.674 | 0.773 | 0.93 | 1.70 | 0.92 | 273(17) | 0.597(078) | 0.914(022) |
| 2.40 | 175(14) | 0.127 | 0.617 | 0.784 | 0.93 | 1.70 | 0.92 | 103.8(8.7) | 0.955(230) | 0.992(040) |
| 3.35 | 77(10) | 0.127 | 0.71 | 0.771 | 0.93 | 1.70 | 0.92 | 28.83(4.09) | 1.073(400) | 1.012(062) |
| 4.35 | 18(5) | 0.127 | 0.706 | 0.69 | 0.93 | 1.70 | 0.92 | 5.891(1.922) | 1.041(730) | 1.007(117) |
| pp: | South | | | | | | | | | |
| 0.63 | 48(7) | 0.128 | 0.348 | 0.658 | 0.99 | 208 | 0.74 | 3.420(511) | | |
| 1.46 | 43(7) | 0.128 | 0.324 | 0.654 | 0.99 | 208 | 0.74 | 1.103(182) | | |
| 2.40 | 15(5) | 0.128 | 0.293 | 0.659 | 0.99 | 208 | 0.74 | 0.253(085) | | |
| 3.35 | 7(3) | 0.128 | 0.359 | 0.64 | 0.99 | 208 | 0.74 | 0.071(031) | | |
| 4.35 | 2(2) | 0.128 | 0.465 | 0.606 | 0.99 | 208 | 0.74 | 0.013(013) | | |
| pp: | North | | | | | | | | | |
| 0.63 | 121(12) | 0.127 | 0.675 | 0.86 | 0.95 | 185 | 0.74 | 3.354(339) | | |
| 1.46 | 124(12) | 0.127 | 0.655 | 0.862 | 0.95 | 185 | 0.74 | 1.178(115) | | |
| 2.40 | 47(9) | 0.127 | 0.614 | 0.87 | 0.95 | 185 | 0.74 | 0.283(055) | | |
| 3.35 | 17(5) | 0.127 | 0.693 | 0.843 | 0.95 | 185 | 0.74 | 0.067(020) | | |
| 4.35 | 4(2) | 0.127 | 0.623 | 0.778 | 0.95 | 185 | 0.74 | 0.015(008) | | |
| pp: | Mean | | | | | | | | | |
| 0.63 | | | | | | | | 3.374(393) | | |
| 1.46 | | | | | | | | 1.158(133) | | |
| 2.40 | | | | | | | | 0.276(062) | | |
| 3.35 | | | | | | | | 0.068(024) | | |
| 4.35 | | | | | | | | 0.014(009) | | |

Table 23: Calculation of the cross sections and ratios versus $p_T$ for the two muon arms. The pp average cross section used to form the ratios assuming symmetry around y=0 is shown at the bottom. The quantities in the third and fourth columns are from 16, $\varepsilon_{BLT}$ is the luminosity weighted average of the 1D1S and 2D trigger efficiencies, and $L$ is the total luminosity for both triggers. The differential cross section shown is $1/(2\pi p_T) * BR * d^2\sigma/dydp_T$ in $nb/(GeV/c)^2$.

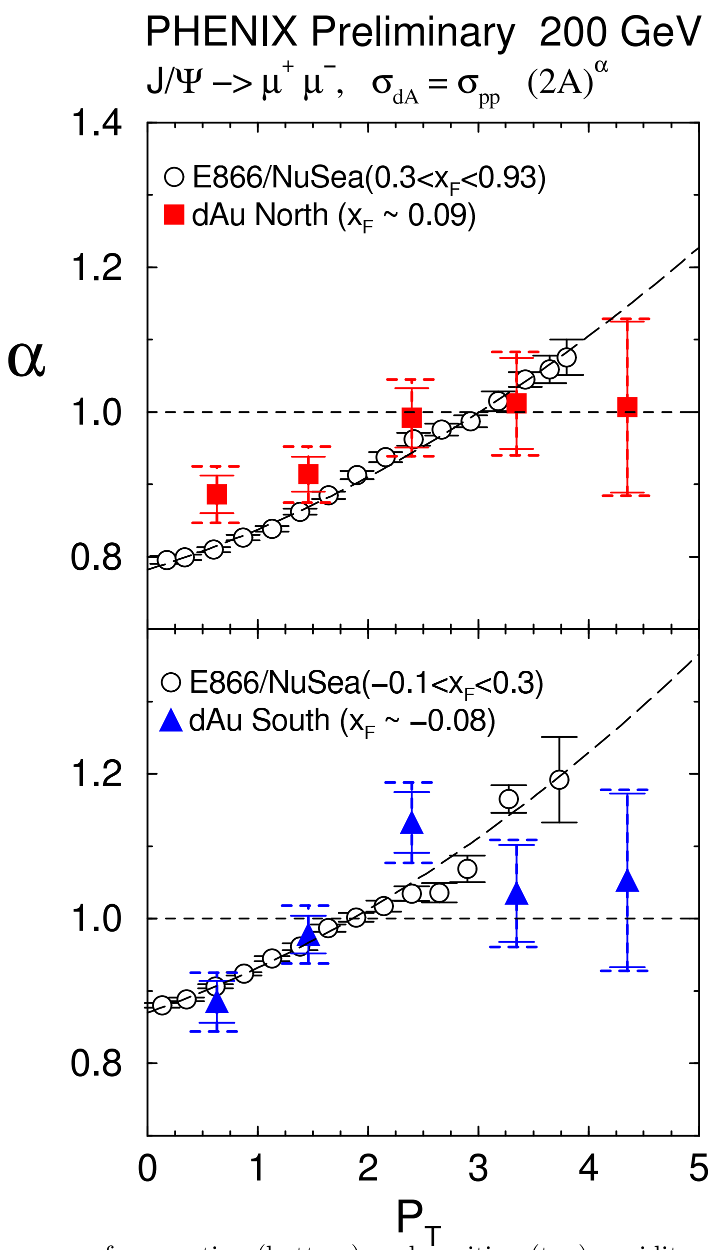


Figure 18: Alpha versus $p_T$ for negative (bottom) and positive (top) rapidity compared to results from E866/NuSea, a lower energy ($\sqrt{s}$ = 38 GeV) fixed target experiment. Solid error bars represent statistical + point-to-point systematics, while the dashed error bars include arm-to-arm errors. A global 2.2 % error bar is not displayed (see tables 19 and 21).

| Bin | $N_{coll}$ | $N_{J/\psi}$ | Width | Bias | $L$ $(nb^{-1})$ | $BR * d\sigma_{J/\psi}$ $(nb)$ | RdA | Rcp |
|---|---|---|---|---|---|---|---|---|
| dAu: | South | | | | | | | |
| MB | 8.4 | 578(27) | 1 | 1 | 1.43 | 10.48(49) | 1.001(047) | |
| 0-20% | 15 | 288(20) | 0.2 | 1 | 1.43 | 26.11(1.81) | 1.285(089) | 1.944(135) |
| 20-40% | 10.4 | 168(14) | 0.2 | 0.995 | 1.43 | 15.31(1.28) | 1.075(090) | 1.627(136) |
| 40-60% | 6.9 | 81(11) | 0.2 | 0.974 | 1.43 | 7.540(1.024) | 0.765(104) | 1.158(157) |
| 60-88% | 3.2 | 50(9) | 0.28 | 0.885 | 1.43 | 3.659(659) | 0.661(119) | 1.000(180) |
| NTag | 3.6 | 58(8) | 0.168 | | 1.43 | 6.260(863) | 1.457(201) | |
| dAu: | North | | | | | | | |
| MB | 8.4 | 784(31) | 1 | 1 | 1.70 | 7.012(277) | 0.670(026) | |
| 0-20% | 15 | 287(19) | 0.2 | 1 | 1.70 | 12.834(850) | 0.631(042) | 0.828(055) |
| 20-40% | 10.4 | 241(17) | 0.2 | 0.995 | 1.70 | 10.831(764) | 0.761(054) | 0.998(070) |
| 40-60% | 6.9 | 146(14) | 0.2 | 0.974 | 1.70 | 6.703(643) | 0.680(065) | 0.892(086) |
| 60-88% | 3.2 | 117(12) | 0.28 | 0.885 | 1.70 | 4.223(433) | 0.763(078) | 1.000(103) |
| NTag | 3.6 | 80(10) | 0.168 | | 1.70 | 0.949(119) | 0.991(124) | |
| pp: | South | | | | | | | |
| | | 118(12) | | | 208 | 0.734(184) | | |
| pp: | North | | | | | | | |
| | | 290(19) | | | 185 | 0.677(161) | | |
| pp: | Mean | | | | | | | |
| | | | | | | 0.692(163) | | |

Table 24: Calculation of the cross sections and ratios versus centrality for the two muon arms using Equation 7. The pp average cross section used to form the ratios assuming symmetry around y=0 is shown at the bottom.

| Arm | Cent. | All | 2D | 1D1S | 2D−1D1S | sigmas |
|---|---|---|---|---|---|---|
| S | 0-20 | 1.944(135) | 1.635(143) | 2.14(160) | −0.505(215) | −2.35 |
| S | 20-40 | 1.627(136) | 2.980(426)BF | 1.083(127) | 1.897(445) | 4.27 |
| S | 40-60 | 1.158(157) | 1.374(223) | 1.166(169) | 0.208(280) | 0.74 |
| S | 60-88 | 1 | 1 | 1 | 0.0 | 0.0 |
| N | 0-20 | 0.828(055) | 0.746(078) | 0.827(067) | −0.081(103) | −0.79 |
| N | 20-40 | 0.998(070) | 1.006(121) | 0.969(082) | 0.037(146) | 0.25 |
| N | 40-60 | 0.892(086) | 0.921(124) | 0.815(111) | 0.106(166) | 0.635 |
| N | 60-88 | 1 | 1 | 1 | 0.0 | 0.0 |

Table 25: Rcp for all runs, runs with deep-deep (2D) trigger only, and runs with deep-shallow (1D1S) only for both north and south muon arms. The difference in Rcp between the trigger subsamples is also determined, together with its number of standard deviation (statistical error only). The “BF” is a bin with a bad fit for the yield. Uncertainties are only statistical from the fits.

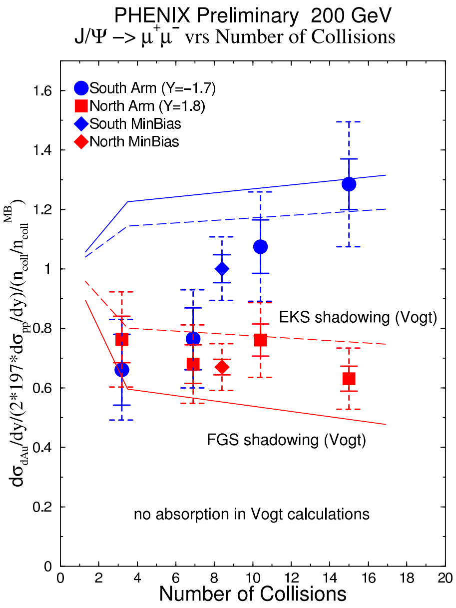


Figure 19: Ratio of per nucleon cross sections versus centrality as indicated by number of collisions. Solid error bars represent statistical + point-to-point systematics, while the dashed error bars include arm-to-arm errors. A global 13.4 % error bar is not displayed (see tables 19, 21 and section 6).

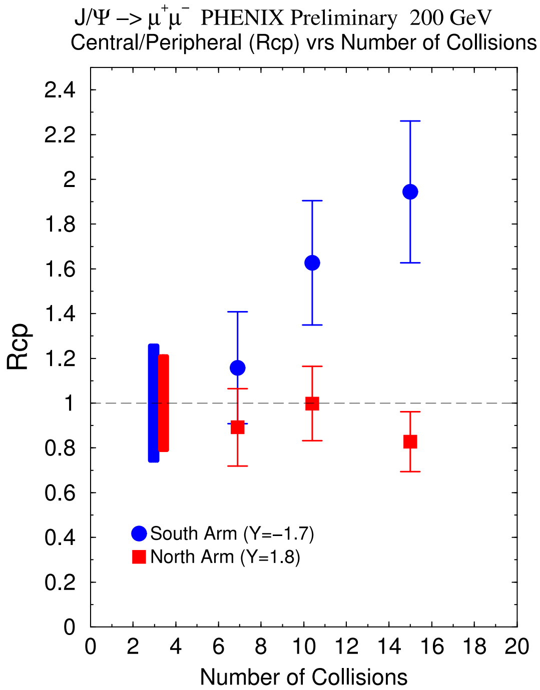


Figure 20: Ratio of cross sections between $J/\psi$'s from more central bins in centrality and the most peripheral bin versus number of collisions. Solid error bars represent statistical + point-to-point systematics, while the dashed error bars include arm-to-arm errors. There is no global error since it cancels in the peripheral/central ratio (see tables 19, 21 and section 6).